DTIC® DEFENSE TECHNICAL INFORMATION CENTER

Information for the Defense Community

DTIC® has determined on 03 / 26 / 2015 that this Technical Document has the Distribution Statement checked below. The current distribution for this document can be found in the DTIC® Technical Report Database.

☑ **DISTRIBUTION STATEMENT A.** Approved for public release; distribution is unlimited.

☐ **© COPYRIGHTED.** U.S. Government or Federal Rights License. All other rights and uses except those permitted by copyright law are reserved by the copyright owner.

☐ **DISTRIBUTION STATEMENT B.** Distribution authorized to U.S. Government agencies only (fill in reason) (date of determination). Other requests for this document shall be referred to (insert controlling DoD office).

☐ **DISTRIBUTION STATEMENT C.** Distribution authorized to U.S. Government Agencies and their contractors (fill in reason) (date determination). Other requests for this document shall be referred to (insert controlling DoD office).

☐ **DISTRIBUTION STATEMENT D.** Distribution authorized to the Department of Defense and U.S. DoD contractors only (fill in reason) (date of determination). Other requests shall be referred to (insert controlling DoD office).

☐ **DISTRIBUTION STATEMENT E.** Distribution authorized to DoD Components only (fill in reason) (date of determination). Other requests shall be referred to (insert controlling DoD office).

☐ **DISTRIBUTION STATEMENT F.** Further dissemination only as directed by (insert controlling DoD office) (date of determination) or higher DoD authority.

Distribution Statement F is also used when a document does not contain a distribution statement and no distribution statement can be determined.

☐ **DISTRIBUTION STATEMENT X.** Distribution authorized to U.S. Government Agencies and private individuals or enterprises eligible to obtain export-controlled technical data in accordance with DoDD 5230.25; (date of determination). DoD Controlling Office is (insert controlling DoD office).

REPORT DOCUMENTATION PAGE

Form Approved
OMB No. 0704-0188

The public reporting burden for this collection of information is estimated to average 1 hour per response, including the time for reviewing instructions, searching existing data sources, gathering and maintaining the data needed, and completing and reviewing the collection of information. Send comments regarding this burden estimate or any other aspect of this collection of information, including suggestions for reducing the burden, to Department of Defense, Washington Headquarters Services, Directorate for Information Operations and Reports (0704-0188), 1215 Jefferson Davis Highway, Suite 1204, Arlington, VA 22202-4302. Respondents should be aware that notwithstanding any other provision of law, no person shall be subject to any penalty for failing to comply with a collection of information if it does not display a currently valid OMB control number.
PLEASE DO NOT RETURN YOUR FORM TO THE ABOVE ADDRESS.

1. REPORT DATE *(DD-MM-YYYY)*	2. REPORT TYPE	3. DATES COVERED *(From - To)*
12/18/2014	Final Technical Report	4/10/2009 - 9/30/2014

4. TITLE AND SUBTITLE
Multi-Energy Processing for Noval Coating Technologies

5a. CONTRACT NUMBER

5b. GRANT NUMBER
N00014-09-1-0943

5c. PROGRAM ELEMENT NUMBER
09PRO7618-00

6. AUTHOR(S)
Lu, Yongfeng

5d. PROJECT NUMBER

5e. TASK NUMBER

5f. WORK UNIT NUMBER

7. PERFORMING ORGANIZATION NAME(S) AND ADDRESS(ES)
University of Nebraska-Lincoln
151 Whittier Research Center, 2200 Vine Street
Lincoln, NE 68583-0861

8. PERFORMING ORGANIZATION REPORT NUMBER
25-1109-0092-001

9. SPONSORING/MONITORING AGENCY NAME(S) AND ADDRESS(ES)
Office of Naval Research
140 Sylvester Road
Bldg 140 Room 218
San Diego, CA 92106-3521

10. SPONSOR/MONITOR'S ACRONYM(S)

11. SPONSOR/MONITOR'S REPORT NUMBER(S)

12. DISTRIBUTION/AVAILABILITY STATEMENT

13. SUPPLEMENTARY NOTES

14. ABSTRACT

Due to the wide range of superior properties, diamonds are of great interest in industry applications and scientific research. The inherent shortcomings of conventional chemical vapor deposition (CVD) methods and the ever-increasing demand for diamonds urge extended efforts for further enhancement of diamond deposition without compromising the diamond quality. Conventional CVD processes, which rely on thermal heating, are inefficient energy coupling routes to drive gas reactions. As an intensive, coherent and monochromatic light, lasers are ideal candidates for exploring alternative energy coupling pathways. To address these challenges, the research efforts mainly focused on laser incorporation in combustion CVD.

15. SUBJECT TERMS

16. SECURITY CLASSIFICATION OF:			17. LIMITATION OF ABSTRACT	18. NUMBER OF PAGES	19a. NAME OF RESPONSIBLE PERSON
a. REPORT	b. ABSTRACT	c. THIS PAGE			Dr. Yongfeng Lu
					19b. TELEPHONE NUMBER *(Include area code)* 402-472-8323

20141229009

University of Nebraska Lincoln

OFFICE OF SPONSORED PROGRAMS

December 18, 2014

Defense Technical Information Center
8725 John J Kingman Road Ste 0944
Fort Belvoir, VA 22060-6218

RE: N00014-09-1-0943 Final Technical Report

Enclosed is the final technical report for the referenced award under the direction of Dr. Yongfeng Lu. If you should have any questions, please address them to Dr. Lu at (402) 472-8323 or by e-mail at ylu2@unl.edu.

Sincerely,

Deb Arent
Assistant Director

151 Whittier Research Center / 2200 Vine Street / P.O. Box 830861 / Lincoln, NE 68583-0861
(402) 472-3171 / FAX (402) 472-9323 / research.unl.edu/sponsoredprograms/

Award Information

Award Number	N000140910943
Title of Research	Multi-energy Processing for Novel Coating Technologies
Principal Investigator	Yongfeng Lu
Organization	University of Nebraska - Lincoln

3. Abstract

Due to the wide range of the superior properties, diamonds are of great interest in industry applications and scientific research. The inherent shortcomings of conventional chemical vapor deposition (CVD) methods and the ever-increasing demand for diamonds urge extended efforts for further enhancement of diamond deposition without compromising the diamond quality. Conventional CVD processes, which rely on thermal heating, are inefficient energy coupling routes to drive gas reactions. As an intensive, coherent and monochromatic light, lasers are ideal candidates for exploring alternative energy coupling pathways. To address these challenges, the research efforts mainly focused on laser incorporation in combustion CVD of diamond films, which led to: 1) promoted energy coupling efficiency; 2) enhanced diamond deposition; 3) controlled crystallographic orientations; and 4) identified roles of active species in combustion CVD of diamond films.

Pure diamond and nitrogen(N)-doped diamond films were deposited using combustion flames assisted by infrared-laser (IR-laser) vibrational excitations of ethylene and ammonia (NH_3) molecules, respectively. Vibrational excitations of precursor molecules were realized using a kilowatt wavelength-tunable CO_2 laser with a spectrum range from 9.2 to 10.9 μm. On-resonance excitation of the CH_2-wagging mode of ethylene (C_2H_4) molecules was demonstrated to be more efficient than off-resonance excitations in promoting the deposition rate and improving the diamond quality, attributed to a higher energy coupling efficiency. Ro-vibrational excitations of C_2H_4 molecules enabled crystallographic control in {100}-textured diamond film deposition. Micro-crystalline N-doped diamond films with a high doping concentration were deposited using an ammonia-added oxyacetylene flame assisted by IR-laser vibrational excitations of the NH-wagging mode of NH_3 molecules.

Optical emission spectroscopy and mass spectrometry were performed to achieve an in-depth understanding of laser effects on diamond deposition and to identify active species roles in diamond formation.

4. Technical section

4.1 Technical objectives

In the period of 2013-2014, the objective of the research was to develop laser-assisted processing techniques for synthesizing diamond by interfering vibrational and ro-vibrational states of precursor molecules using laser beams of matching wavelengths. The research efforts mainly focused on the following four tasks: 1) diamond deposition using combustion flames assisted by on- and off-resonance vibrational excitations of C_2H_4 molecules; 2) controlled growth of {100}-textured diamond films using combustion flames assisted by ro-vibrational excitations of C_2H_4 molecules; 3) micro-crystalline N-doped diamond film deposition with laser resonant vibrational excitations of NH_3 molecules; and 4) investigation of roles of active chemical in the diamond growth.

4.2. Technical approaches

I. Introduction of experimental methods

i. Sample preparation

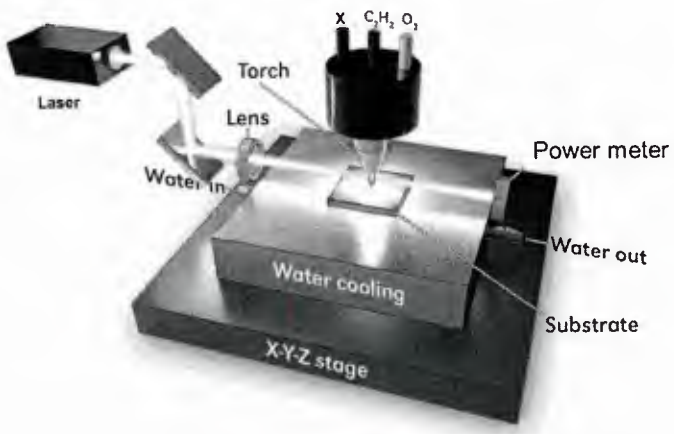

Figure 1.1 Laser-assisted combustion CVD setup for diamond deposition.

Figure 1.1 shows a schematic experimental setup of the laser-assisted combustion CVD system. The combustion flame was produced by a gas mixture of X (C_2H_4 or NH_3), C_2H_2, and O_2. X was added due to its strong IR activities, which is capable of effectively coupling IR-laser energy via resonant vibrational excitations. A wavelength-tunable continuous-wave (CW) CO_2 laser (PRC Inc, 9.2 ~ 10.9 μm) was used as the irradiation source. The laser beam irradiated the flame in a direction normal to the flame axis but parallel with the substrate surface. The IR-laser beam was focused using a ZnSe lens (focal length = 25.4 cm) to ~ 2 mm in diameter, which is the same as the average diameter of the inner flame. A tungsten carbide (WC) substrate (BS-6S, Basic Carbide Corp.) with a dimension of 25.4 × 25.4 × 1.6 mm^3 and a cobalt composition of 6% was placed on a water-cooled brass plate, which was mounted on a motorized X-Y-Z stage. The distance between the substrate surface and the inner flame was around 0.5 mm. The temperature of the substrate during the deposition was maintained at 770 ~ 780 °C and monitored by a

noncontact pyrometer (OS3752, Omega Engineering, Inc.).

ii. Diamond characterizations

Raman spectroscopy: Raman spectroscopy is widely used to characterize carbon material. Diamond films prepared in the study were evaluated using a micro-Raman spectrometer (inVia, Renishaw), as shown in **Figure 1.2**(a). An argon-ion (Ar^+) laser with a wavelength of 514.5 nm and a power of 50 mW was used as the exciting source. The beam was focused to a spot of approximately 5 μm using a 20× objective lens.

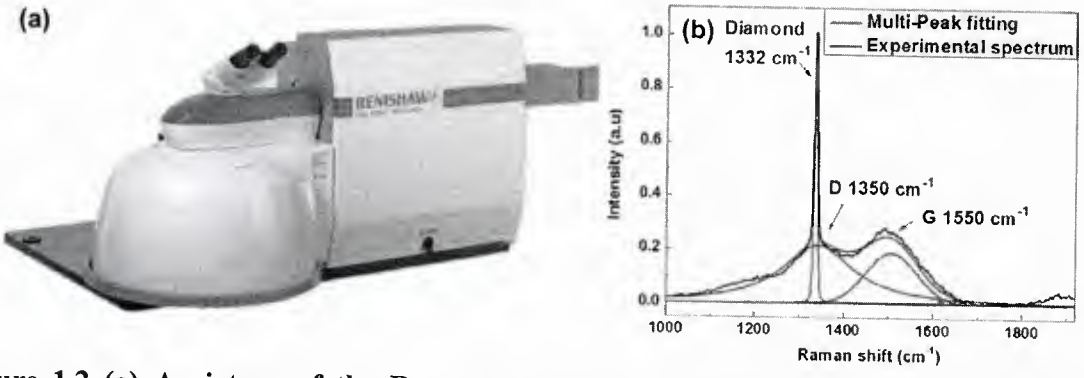

Figure 1.2 (a) A picture of the Raman spectroscopy system (inVia Raman microscopy, Renishaw); (b) A Raman spectrum of a diamond film and its multi-peak fitting curves.

Figure 1.2(b) shows a Raman spectrum (black line) and its multi-peak fitting curves (red line) collected from a sample prepared using the combustion CVD. Three Raman peaks are resolved as 1332, 1350, and 1550 cm^{-1}, respectively. The sharp peak centered at 1332 cm^{-1} arises from sp^3-hybridized bonded carbon and is a typical diamond peak. The band centered at 1350 cm^{-1} (D-band) on the shoulder of the diamond peak is attributed to the breathing modes of sp^2 atoms in rings, reflecting disordered carbon in the film.[1] The broad band centered at 1550 cm^{-1} (G-band) is attributed to the bond stretching of all pairs of sp^2 atoms in both rings and chains, indicating graphitic carbon in diamond matrix.[1] Both D- and G-bands represent non-diamond carbon phase in diamond films. The Raman cross-section of amorphous carbon in comparison with diamond is 1:233 for the 514.5 nm laser excitation. Based on this, quality factor, Q_i, is calculated to evaluate the content of diamond phase in CVD diamond films via a relation:[2]

$$Q_i = \frac{I_{diamond}}{I_{diamond} + \frac{I_{non-diamond}}{233}} \times 100\% \ , \qquad (1.1)$$

where $I_{diamond}$ and $I_{non\text{-}diamond}$ being the integrated intensities of the fitting curves corresponding to the diamond peak and the sum of non-diamond bands (D- and G-band), respectively.

Scanning electron microscopy: Surface morphologies of diamond films prepared were characterized by a scanning electron microscope (SEM; XL-30, Philips Electronics), as shown in **Figure 1.3**(a). **Figure 1.3**(b) and (c) show two SEM images of a {100}-oriented and a random-oriented diamond film, respectively.

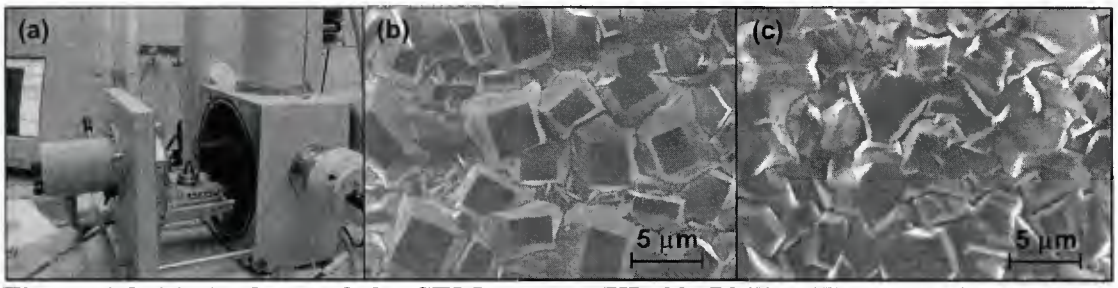

Figure 1.3 (a) A photo of the SEM system (XL-30, Philips Electronics) and SEM images of (b) a {100}-oriented diamond film and (c) a random-oriented diamond film.

Stylus profile: Stylus profiler is an instrument used to measure surface profiles, the film thickness, and surface roughness. **Figure 1.4**(a) shows a photo of the stylus profiler (XP-2, AMBiOS) used. The stepping speed is 0.05 mm/s. **Figure 1.4**(b) shows a typical film thickness profile of a CVD diamond film. A diamond film deposited using combustion CVD exhibits a radius inhomogeneous profile caused by the radius distribution of heat and species flux. A diamond deposition rate is calculated via dividing a film thickness by a deposition time.

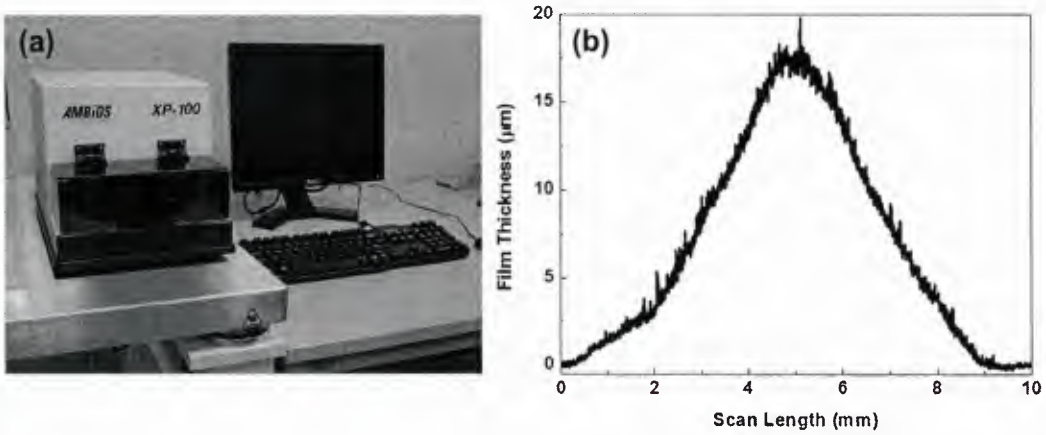

Figure 1.4 (a) A photo of the stylus profiler (XP-2, AMBiOS) and (b) a typical film thickness profile of a CVD diamond film.

iii. Combustion flame diagnostics

Optical emission spectroscopy (OES): OES were performed to verify the radical distribution in the flames. The setup for the OES study is shown in **Figure 1.5**. Optical emission spectra of flames were collected during the diamond deposition in a direction normal to the flame axis. A UV grade quartz lens (15 cm) was used to image the flame onto the slit panel of the spectrometer (Andor Sharmrock SR-303i-A). An intensified charge-coupled device (ICCD, Andor iStar DH-712) was used to collect the spectrum information. The wide-range spectra were obtained using a grating of 150 lines/mm from the position 0.5 mm under the inner flame tip while the high-resonation spectra for flame temperature measurements were obtained using a grating of 2400 lines/mm from the middle part of the inner flame. All spectra were taken with a horizontal slit width of 50 μm centered at the tip apex of the inner flame. The flame images taken were

proportional to the real flames in size. A background spectrum was taken before the collections of the emission spectra and subtracted from all captured spectra.

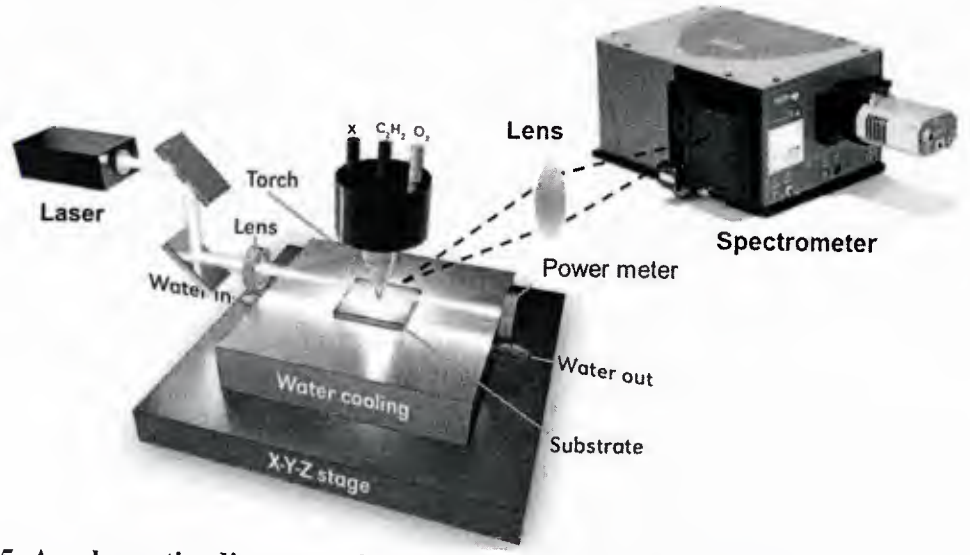

Figure 1.5 A schematic diagram of optical emission spectroscopy of the laser-assisted diamond combustion CVD system.

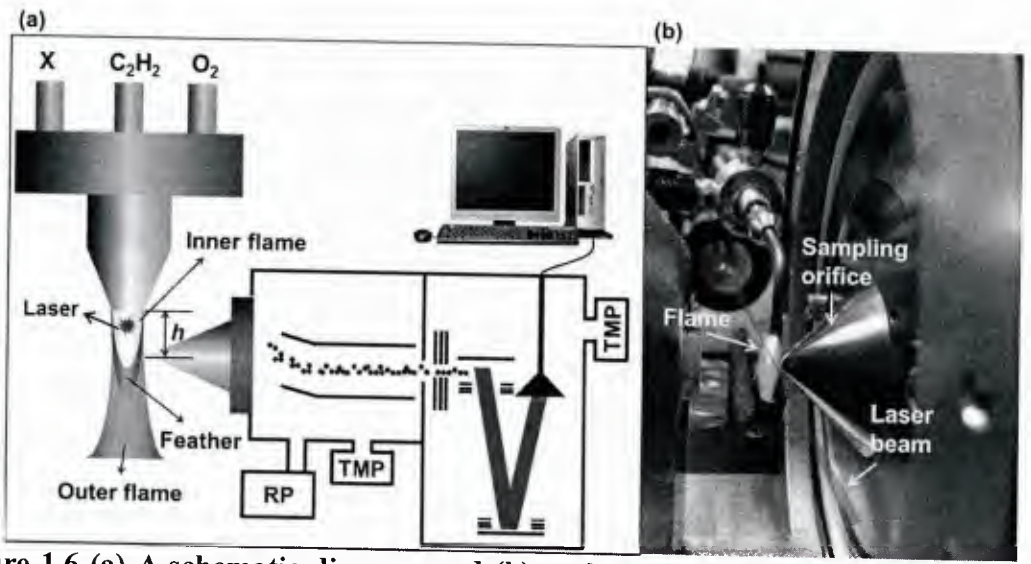

Figure 1.6 (a) A schematic diagram and (b) a photo of the setup of mass spectrometry of combustion flames

Mass spectrometry (MS): Ionization of intermediates occurs in the combustion flames, making the flames suitable for direct analysis using MS. MS was carried out to simultaneously detect both positive and negative ions to understand the flame chemistry. The experimental setup for the MS studies is schematically shown in **Figure 1.6**(a). **Figure 1.6**(b) shows a photo of the MS system of combustion flames. Ions in the flames were detected using a time-of-flight mass spectrometer (MS, AccuTOF^{TM}, JEOL USA, Inc.). A stainless steel orifice with an inner diameter of 400 μm was used to collect ions from the flames in open air. A CO_2 laser beam was normally

projected through the flame at the torch nozzle with a focused diameter of ~ 2 mm. The incident laser power was 100 W. The combustion torch was fixed on a motorized 3D stage. The relative position of the flames to the orifice was precisely controlled with a resolution of 2.5 μm. The mass range was from 10 to 60 m/z. The MS data were analyzed using the TSSPro software (Shrader Analytical and Consulting Laboratories, Inc. Version 3.0) and the MS Tools software (JEOL USA, Inc.). To eliminate the variation of the absolute value in different measurements, relative concentrations of ions, *c*, are calculated from Eq (1.2),

$$c = RIC/TIC \quad , \tag{1.2}$$

where *RIC* and *TIC* being the reconstructed ion counts of selected ions and total ion counts, respectively.

II. Enhanced diamond deposition with resonant vibrational excitations of ethylene molecules

i. Experimental details

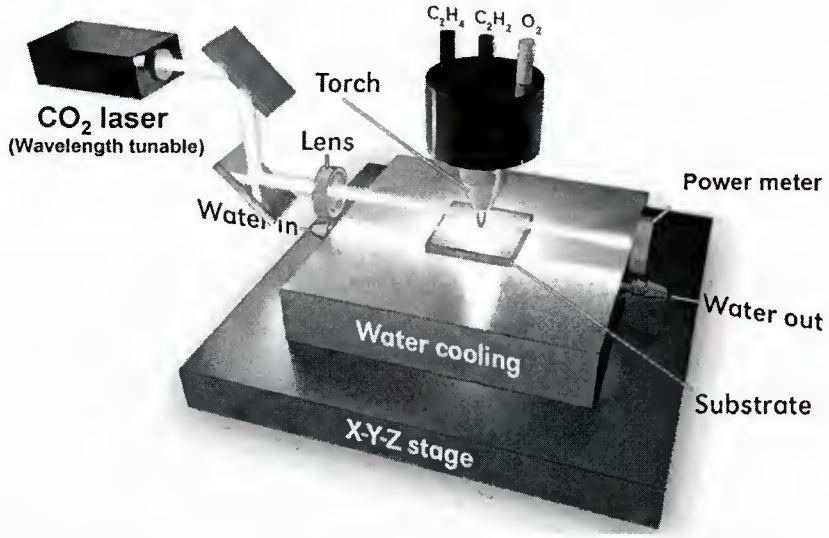

Figure 2.1 IR-laser assisted combustion CVD setup for diamond film deposition.

Figure 2.1 shows a schematic experimental setup of the IR-laser-assisted combustion CVD system. The combustion flame was produced by a gas mixture of C_2H_4, acetylene (C_2H_2), and oxygen (O_2) with flow rates of 0.62, 0.62, and 1.2 standard liters per minute (slm), respectively. C_2H_4 was added into the flame due to its strong infrared activities, which was capable of effectively coupling laser energy into the reaction system due to vibrational excitations. A wavelength-tunable CW CO_2 laser (PRC Inc, 9.2~10.9 μm) was used as the irradiation source. Based on the available emission lines in the CW CO_2 laser, the CH_2-wagging mode (a Type c fundamental band, υ_7, at 949.3 cm^{-1}) of C_2H_4 molecules was selected for the investigation. Laser irradiations with five different wavelengths centered at 10.532 μm, including 10.494, 10.513, 10.532, 10.551 and 10.571 μm, were selected to irradiate the $C_2H_4/C_2H_2/O_2$ flame in a direction normal to the flame axis and parallel with the substrate surface. The laser incident power was adjusted to keep the absorbed power to be 20 W for all laser wavelengths. The deposition time was fixed at 1 hour.

As shown in **Figure 2.1**, a power meter was placed in the laser path next to the combustion flame. The absorbed laser power (ΔW) is calculated by subtracting the transmitted laser power (W_o) from the incident laser power (W_i). The laser incident power was tuned to keep the absorbed laser power to be 20 W constantly for all laser wavelengths. An absorption spectrum of the gaseous C_2H_4 was collected in a vacuum absorption cell at room temperature. The cell was vacuumed to a base pressure of 3.06×10^{-2} Torr. C_2H_4 gas diluted in nitrogen was fed into the chamber at a total pressure of 100 Torr. The partial pressure of C_2H_4 was 10 Torr. The incident laser power was 100 W. The laser power before and after passing through the chamber was measured. The laser energy absorption rate is calculated by dividing the absorbed laser power by the incident laser power.

ii. Results and discussion

Figure 2.2 shows the CO_2 energy absorption spectrum of the $C_2H_4/C_2H_2/O_2$ flame. Two predominant peaks are resolved, an intensive peak at 10.532 μm and a weak one at 10.22 μm. Both of them are attributed to the same vibrational mode of C_2H_4, the out-of-plane B_{1u}-species CH_2-wagging vibration mode (ν_7).[3]

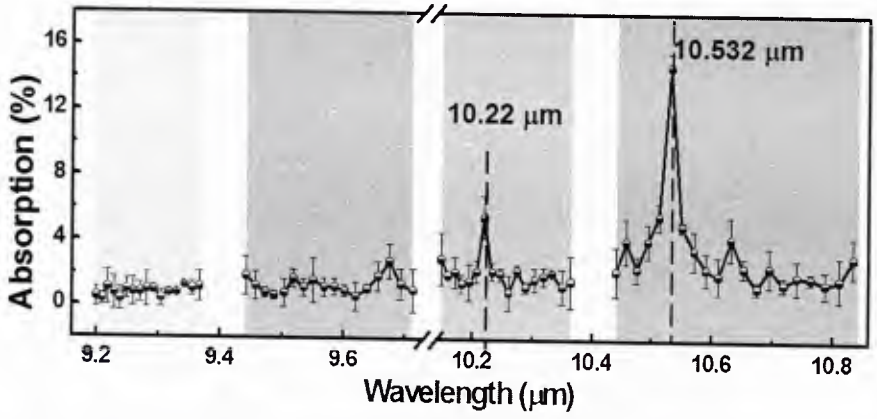

Figure 2.2 A CO_2 laser energy absorption spectrum of the $C_2H_4/C_2H_2/O_2$ flame, ranging from 9.2 to 10.9 μm. The colored bars indicate four CO_2 laser emission bands.

In the CH_2-wagging mode of C_2H_4 molecules, the C and H planes bounce up and down relative to each other. The molecule vibrates look like a butterfly as illustrated in **Figure 2.3**. Under laser irradiation with a matching wavelength, the vibration is resonantly excited. The intensive absorption peak at 10.532 μm (equivalent to 949.48 cm^{-1}) is attributed to a strong resonance to the fundamental Q band head (949.3 cm^{-1}) of the CH_2-wagging vibration mode.[3] The weak absorption peak at 10.22 μm (equivalent to 978.47 cm^{-1}) results from a match to one ro-vibrational sub-band head (978.94 cm^{-1}) of the same mode. In this work, the influence of on- and off-resonance excitations of the fundamental Q band of the CH_2-wagging mode on diamond deposition was investigated.

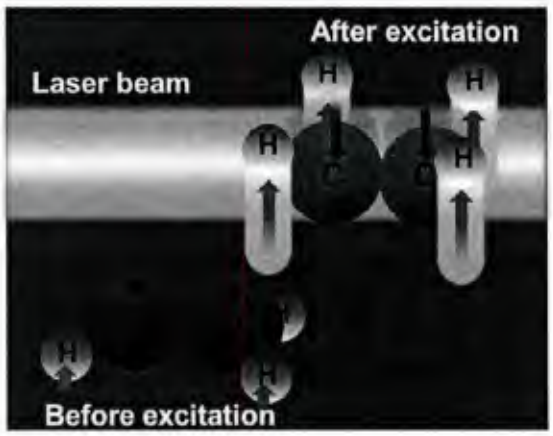

Figure 2.3 A schematic illustration of the CH_2-wagging mode of ethylene without and with laser resonant excitations.

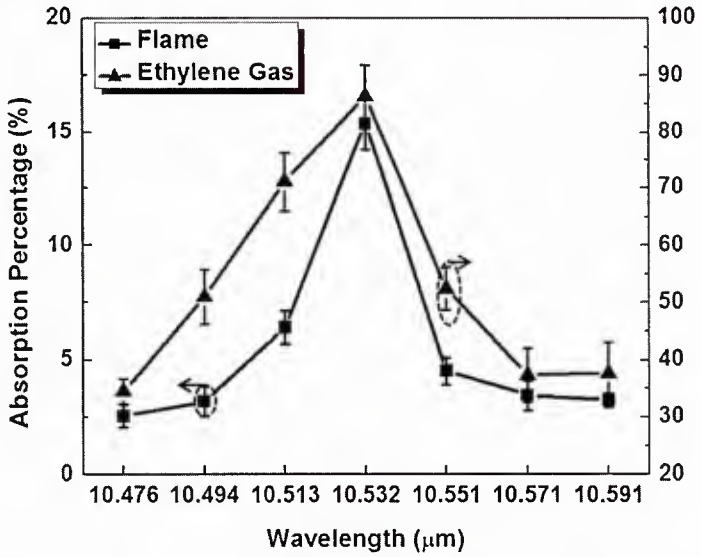

Figure 2.4 A absorption spectrum of CO_2 laser energy by $C_2H_4/C_2H_2/O_2$ flames (black solid squares) and C_2H_4 gas (blue solid triangles), ranging from 10.476 to 10.591 μm.

Figure 2.4 zooms into the region of interest, showing the CO_2 laser energy absorption spectra of the $C_2H_4/C_2H_2/O_2$ flame (black solid squares) and C_2H_4 gas (blue solid triangles) at room temperature, respectively, ranging from 10.476 to 10.591 μm. The absorption spectra of the flame and the C_2H_4 gas exhibit the same absorption peak at 10.532 μm, which confirms that the laser energy is coupled through C_2H_4. The flame absorption increases from 3 to 15.2% when the laser wavelength is tuned from 10.476 to 10.532 μm and then drops to 3.2% as the laser wavelength is tuned from 10.532 to 10.591 μm. The absorption of CO_2 laser energy in the wavelength range from 10.476 to 10.591 μm locates in the fundamental Q band of the v_7 mode of ethylene molecules.[3] The absorption peak at 10.532 μm (equivalent to 949.48 cm^{-1}) is attributed to the strong vibrational resonance of the v_7 fundamental band (949.3 cm^{-1}). The laser excitation at 10.532 μm is therefore named as "on-resonance" laser excitation. Centered at 949.3 cm^{-1}, the v_7 band consists of a broad range of quantized rotational sub-bands due to the rotational partition function, including the *R* branches (from 986.23 to 1151.01 cm^{-1}) and *P* branches (from 869.38

to 911.57 cm^{-1}), covering a corresponding wavelength range from 8.688 to 11.502 μm.[3] The rotational sub-band structure allows the absorption of laser energy in a wide wavelength range centered at 10.532 μm. The laser irradiations at wavelengths other than 10.532 μm, including 10.494, 10.513, 10.551 and 10.571 μm, are termed as "off-resonance" excitations. At the off-resonance excitations, laser energy is coupled through the ro-vibrational transitions of the v_7 mode but with decreased absorption rates as the $\Delta\lambda=|\lambda_{laser}-\lambda_{v7}|$ increases. The absorption intensity is decided by the population in the initial state of the transition. Therefore, the absorption intensity, as shown in **Figure 2.4**, decreases substantially when the incident laser wavelength is tuned away from the central vibrational band at 949.3 cm^{-1} due to the decreased population in the initial state involved in the ro-vibrational transition. To achieve the same absorbed power, 20 W, a higher laser incident power is required when shifting away from the resonant wavelength of 10.532 μm.

Morphologies and grain sizes of the diamond films deposited with excitations at different laser wavelengths are shown in **Figure 2.5**. The diamond film deposited without laser irradiation consisted of randomly oriented grains with an average size of 2.6 μm, as shown in **Figure 2.5**(a). After introducing the CO_2 laser excitation at 10.494 μm, larger diamond crystals were observed in the center area of the films, as shown in **Figure 2.5**(b). The diamond grain size increased as the laser wavelength approached to 10.532 μm and reached a maximum value of 14.3 μm at 10.532 μm, **Figure 2.5**(d). As the wavelength was further tuned to 10.571 μm, the diamond grain size declined to 3.4 μm, **Figure 2.5**(e) and (f).

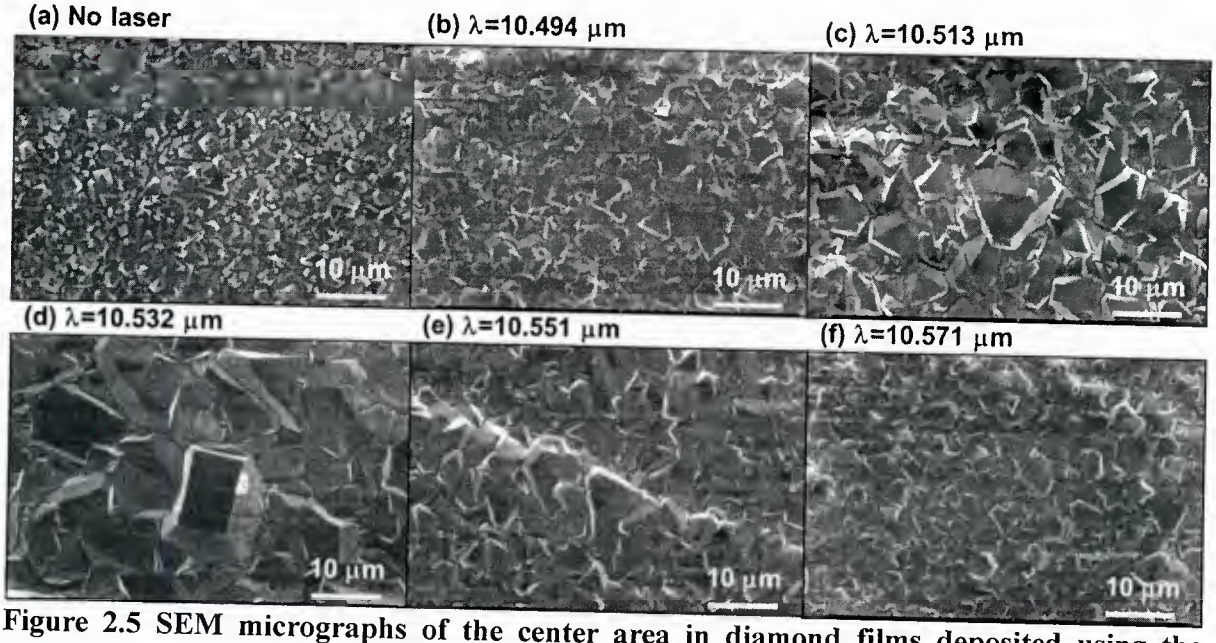

Figure 2.5 SEM micrographs of the center area in diamond films deposited using the $C_2H_4/C_2H_2/O_2$ flame with CO_2 laser excitations: (a) no laser excitation, at (b) 10.494, (c) 10.513, (d) 10.532, (e) 10.551, and (f) 10.571 μm. The absorbed laser power was 20 W for all laser wavelengths.

The diamond film thicknesses were measured using a stylus profiler. The deposition rates were calculated by dividing the film thicknesses by the deposition time and plotted with respect to laser wavelengths in **Figure 2.6**. The diamond deposition rate without laser irradiation was 7.2

μm/hr. The highest deposition rate, 40.8 μm/hr, was obtained at 10.532 μm, which gradually decreased as the laser wavelength was tuned away from the central vibrational band. The deposition rate was enhanced by a factor of 5.7 with the resonant excitation at 10.532 compared with that without laser irradiation. The fivefold increase in the diamond deposition rate indicates that the diamond growth is significantly enhanced with the resonant excitations.

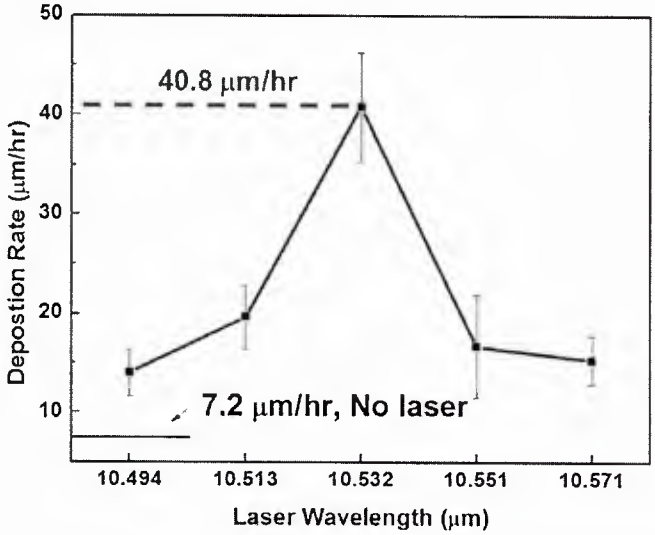

Figure 2.6 Deposition rate as a function of the laser wavelengths.

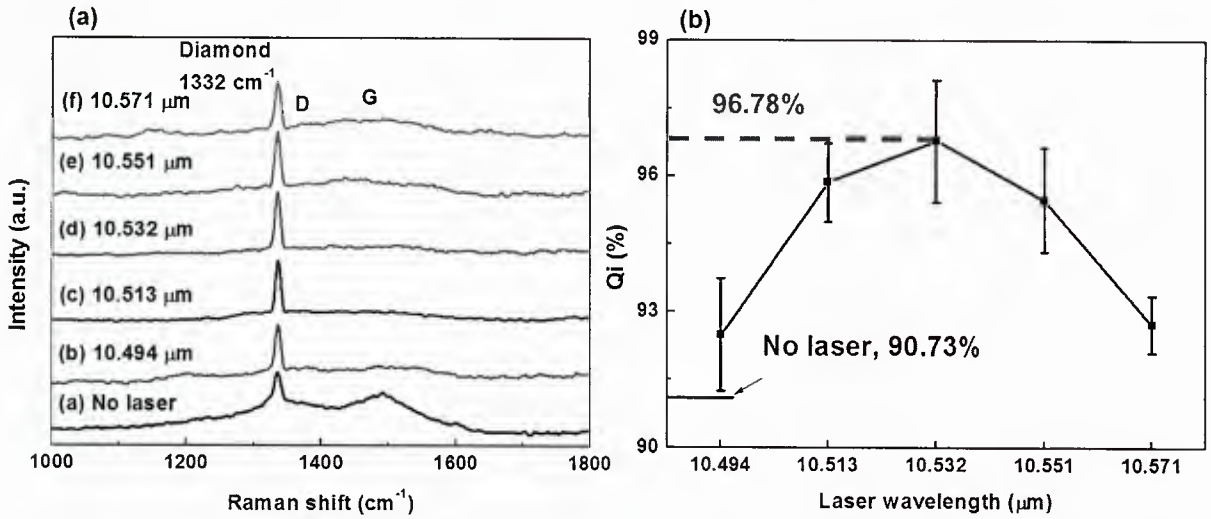

Figure 2.7 (a) Raman spectra of diamond films deposited using $C_2H_4/C_2H_2/O_2$ flames without laser excitations and with CO_2 laser excitations at different laser wavelengths; (b) the diamond quality index factors of the diamond films plotted as a function of laser wavelengths.

The bonding structures in the diamond films were characterized using Raman spectroscopy as shown in **Figure 2.7**(a). Three Raman peaks were resolved: a diamond peak at 1332 cm^{-1}, a weak D-band centered at 1350 cm^{-1}, and a broad G-band centered at 1550 cm^{-1}. The sample deposited without laser excitation exhibited a strong G-band and a relatively weak diamond peak (see

Spectrum (a)). With the laser excitation at 10.494 μm, the diamond peak became slightly stronger associated with a weakened G-band (see Spectrum (b)). As the laser wavelength getting close to 10.532 μm, the diamond peak intensity increased whereas G-band intensity decreased further. As shown in Spectrum (d), the G-band of the diamond film deposited under the laser excitation at 10.532 μm was almost invisible, indicating a pure diamond phase. As the wavelength was further tuned from 10.551 to 10.571 μm, the diamond peak broadened and weakened while G-band intensity increased again. Diamond quality factors are retrieved from the Raman spectra following the relation described in Section I and plotted as a function of laser wavelengths in **Figure 2.7**(b). The diamond quality factor curve showed a similar trend to the deposition rate curve in **Figure 2.6**. The diamond film obtained with the laser excitation at 10.532 μm had the highest diamond quality factor value, 96.78%, which is 6.05% higher than that without laser excitation. Considering the absorbed laser power by the flame was the same for all laser wavelengths, the increases in the diamond grain sizes, film deposition rates, and diamond quality index factors indicate that the diamond growth was significantly promoted under the laser-assisted resonant vibrational excitation of C_2H_4 molecules.

Spectroscopic investigation was carried to study the $C_2H_4/C_2H_2/O_2$ flames with and without the IR-laser irradiation. **Figure 2.8** shows optical images of the $C_2H_4/C_2H_2/O_2$ flames under laser irradiation at different laser wavelengths. The length of the inner flame was about 5 mm without the laser irradiation. Under IR-laser irradiation, the inner flame became brighter and started to shrink in length and expanded in diameter, indicating an accelerated combustion reaction process induced by the laser energy coupling. From 10.476 to 10.532 μm, the inner flame shrank continuously in length and expanded in diameter. When the wavelength was tuned from 10.532 to 10.591 μm, the flame shape bounced back with increased inner flame lengths and reduced diameters. At 10.532 μm, the length of the inner flame was the shortest, 3 mm, with a 57% expansion in diameter as compared with the flame without laser irradiation. The brightest flame was found when the CH_2-wagging mode was resonantly excited at 10.532 μm. As evidenced by the flame shape and brightness, the on-resonance excitation was more effective than off-resonance excitations in laser energy coupling and reaction acceleration.

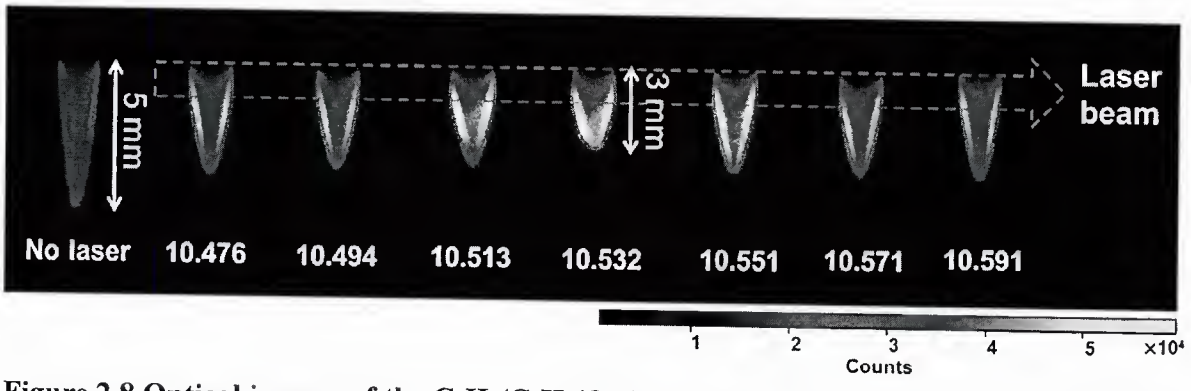

Figure 2.8 Optical images of the $C_2H_4/C_2H_2/O_2$ flames without and with laser excitations at different laser wavelengths.

The rotational temperature, T_r, of molecular species is generally very close to the gas kinetic temperature (flame temperature) due to a strong coupling between translational and rotational energy states.[4] The rotational temperature could be determined using the Boltzmann plot derived from high-resolution rotational emission intensity of species in OES. The electronic transition of

CH [$A^2\Delta$-$X^2\Pi$ (0,0)] was selected to determine the rotational temperature owing to its relatively high emission intensity. **Figure 2.9** shows a typical OES spectrum of the R branch of the CH [$A^2\Delta$-$X^2\Pi$ (0,0)] band (**Figure 2.9**(a)) and the corresponding Boltzmann plot (**Figure 2.9**(b)) derived from the equation:[4]

$$\ln\left(\frac{I\lambda^4}{S_{J'J''}}\right) = -\frac{1}{T_r}\frac{E_{J'}}{k} + lnC, \tag{2.1}$$

where I is the relative emission intensity of a rotational line obtained from the experimental spectrum, C is a proportional constant which is the same for all rotational transitions within a band, $S_{J'J''}$ is the rotational intensity factor, λ is the wavelength of the emitted spectral line, $E_{J'}$ is the rotational energy of the initial level, k is the Boltzmann constant, and T_r is the rotational temperature. The value of $S_{J'J''}$ and $E_{J'}$ are given in Ref.[4]. The value $-1/T_r$ is the slope of the Boltzmann plot of $ln\left(\frac{I\lambda^4}{S_{J'J''}}\right)$ versus $\frac{E_{J'}}{k_B}$.

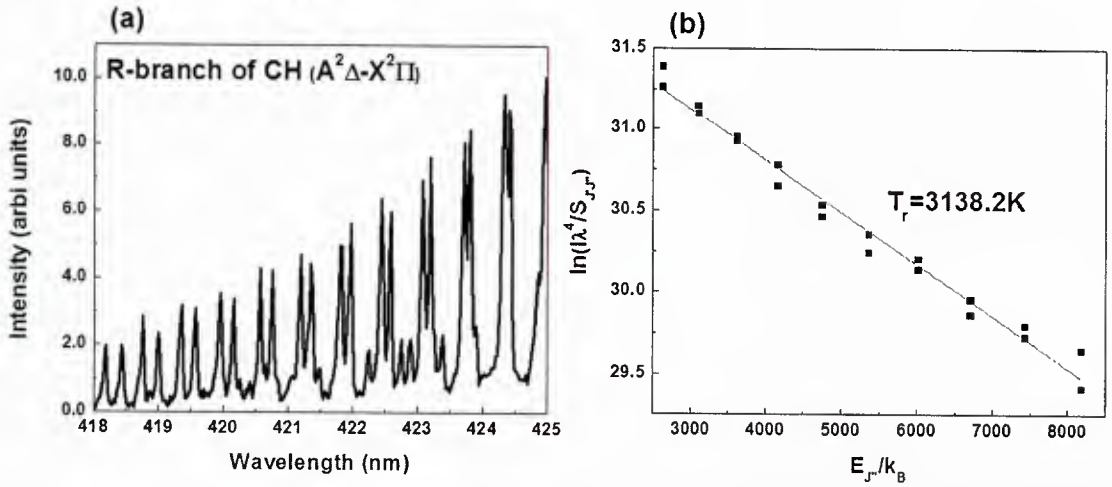

Figure 2.9 (a) The R branch of the CH band [$A^2\Delta$-$X^2\Pi$ (0,0)] used in flame temperature calculation; (b) Boltzmann plot to obtain the rotational temperatures with the laser excitation at 10.532 μm.

Figure 2.10 shows the calculated CH rotational temperature from the middle part of the inner flame with respect to the laser wavelength. The calculated rotational temperature curve was consistent with the flame brightness as displayed in **Figure 2.8**. Compared with the off-resonance excitations, the on-resonance excitation of the CH_2-wagging mode led to the highest flame temperature even with the same amount of laser power coupled into the flames. The CH rotational temperature increased from 2886 K (without laser irradiation) to 3000 K (laser irradiation at 10.476 μm), reached the highest point at 3138 K (resonant excitation of the v_7 vibrational band at 10.532 μm), and bounced back to 2925 K (laser irradiation at 10.591 μm).

The flame temperature profile with regard to laser wavelengths suggests that the laser irradiation modified the combustion process in a way that increased the flame temperature. The high flame temperature plays an importance role in enhancing the diamond deposition. At a high temperature (> 3000 K), a significant fraction of hydrogen molecules in the flames are converted

into atomic hydrogen as expressed by the reaction:[5]

$$H_2 \rightarrow \mathrm{H} + \mathrm{H} \tag{2.2}$$

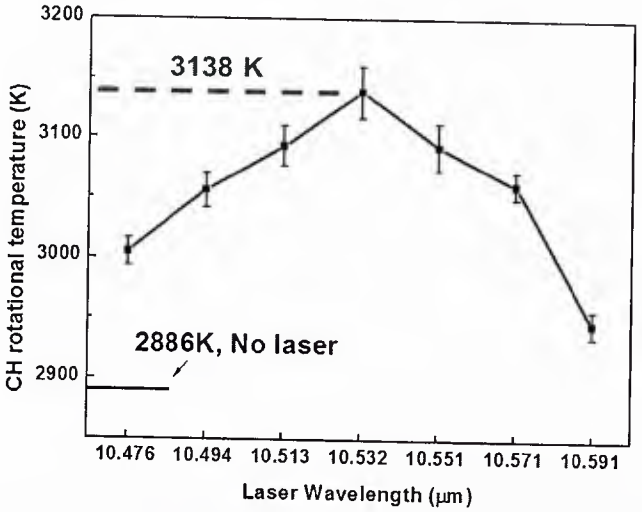

Figure 2.10 The $C_2H_4/C_2H_2/O_2$ flame temperature as a function of laser wavelengths.

The absorption and desorption processes of atomic hydrogens have been widely accepted as essential processes controlling the CVD diamond growth. The degree of the hydrogen dissociation strongly depends on the temperature.[5] The high degree of atomic hydrogen production at the high flame temperature under the on-resonance excitation led to the observed diamond quality improvement and growth rate increase. Two energy coupling processes are suggested to be responsible for the combustion flame temperature increase. One is laser heating effect caused by collisional dissipation. The other one is acceleration of the combustion reactions which are highly exothermic, creating a high-temperature environment. To understand the functions of the coupled laser energy, the flame temperature increase was estimated assuming all the absorbed laser energy deposited to thermally heat the flame using Eq. (2.3):[6]

$$\sum n_i C_{p,i} \frac{dT}{dt} = \Delta Q, \tag{2.3}$$

where n_i and $C_{p,i}$ are the mole and heat capacity of the components in the system, T is the temperature, t is the time and ΔQ is the absorbed laser power.

The flame is a complex system with a large variety of species, which makes the estimation difficult. To simplify the estimation process, the flame temperature increase was estimated for two extreme conditions. One is to assume the precursor gases at the torch nozzle are not ignited at all and the absorbed laser power (20 W) is all deposited to raise the precursor gas temperature; the other one is that all the precursor gases react completely and the absorbed laser power is entirely deposited to increase the temperature of the final products, CO and H_2. For the first case, the flame was treated as a continuous flowing gas mixture of O_2, C_2H_2 and C_2H_4. Assuming all the absorbed laser power deposited to enhance the gas temperature through collisional dissipation processes, the estimated flame temperature increase was 166 K, which is lower than the observed temperature increase, 252 K at 10.532 μm. For the latter case, the reactions of the C_2H_4:C_2H_2:O_2 flames can be expressed as the following equations based on the hydrocarbon-oxygen volume ratio in the precursor mixture:[5]

$$C_2H_2 + O_2 \rightarrow 2CO + H_2 \qquad \Delta H_R^\circ = -107\ kcal/mol \qquad (2.4)$$
$$C_2H_4 + O_2 \rightarrow 2CO + 2H_2 \qquad \Delta H_R^\circ = -65.3\ kcal/mol \qquad (2.5)$$

The estimated flame temperature was 2958 K, which is close to the actual flame temperature without laser irradiation but lower than the observed temperature of 3138 K at 10.532 μm. According to the estimation, the observed flame temperature increase is obviously higher than the flame temperature increase due to solely thermal heating by the dissipated laser energy. The result indicates that besides the thermal heating process, resonant vibrational excitation of C_2H_4 molecules modified the combustion processes in a way that accelerated the combustion reaction rates. With a higher reaction rate, more C_2H_4 and C_2H_2 molecules were consumed and more heat was generated within the same time frame, which increased the flame temperature and subsequently promoted the diamond synthesis process.

The temperature distribution shows large spatial gradients inside the inner cone of the combustion flame. The gas temperature at the torch nozzle is generally at around several hundred kelvins since the ignition just initiates at this point.[7] As shown in **Figure 2.8**, the brightness at the torch nozzle is much lower than the middle part of the inner flame. The laser beam was directed into the flame at the torch nozzle where the precursor gas temperature (< 1000 K) was much lower than that in the middle of the inner flame (~ 3000 K), as indicated in **Figure 2.8**. Sufficient thermal population in the ground state (v = 0) of C_2H_4 molecules is critical for efficient absorption of the incident IR photons. The thermal population of the C_2H_4 molecules in the ground state (v = 0) is calculated at different gas temperatures using Boltzmann Eq. (2.6):

$$\frac{N_{v=0}}{N} = \frac{e^{-\frac{E_{v=0}}{kT}}}{\sum_i e^{-\frac{E_i}{kT}}} \qquad (2.6)$$

where $N_{v=0}$ and $E_{v=0}$ are the molecular population and the state energy at the ground state (v = 0), N is the total molecular population, k is the Boltzmann constant, T is the gas temperature, and E_i is the state energy. All 12 vibrational modes of C_2H_4 were considered in the calculation. According to the calculation, the thermal population percentages of molecules at the ground state (v = 0) were 94.66%, 15.75%, 0.03% at 300, 1000 and 3000 K, respectively. Considering the laser beam was directed at the torch nozzle where the gas temperature was lower than 1000 K, the fraction of molecules available for laser excitation at v = 0 was higher than 15.75%.

Strong emissions from C_2 and CH radicals were observed in the visible range in all the acquired OES spectra of the flames with laser irradiations at different laser wavelengths as shown in **Figure 2.11**(a). A weak emission peak of OH was detected at around 320 nm. Obvious increase in the absolute emission intensities of CH and C_2 radicals was observed in the laser-irradiated flames. The emission intensities of these species kept increasing as the laser wavelength approached to 10.532 μm, indicating combustion reactions became more intensified. OES analysis of the flames was valuable to determine the evolvement of relative species concentrations under different excitation conditions, given that the variation of integrated intensity of species emission peaks is proportional to the related species population. Relative species concentrations are calculated by dividing the integrated intensity of species emission peaks by the integrated intensity of the whole spectrum, which are plotted as a function of laser

wavelengths in **Figure 2.11**(b). The C_2 relative concentration increased as laser wavelengths was tuned closer to 10.532 μm, reaching a maximum value at 10.532 μm while the CH and OH relative concentrations were found to be minimal. The different change trend of these three species indicates laser resonant excitations efficiently steered the combustion process in the flames. This result was consistent with previous reports.[8] It was noted a strong relation between the C_2 concentration profile and the diamond deposition rate.[8] The insertion of a carbon dimer, C_2, into a C=C double bond leads to carbine structure, which in turn induces secondary nucleation and a fast deposition rate.[9] The maximum value of C_2 concentration explains the high deposition rate at 10.532 μm. Although C_2 was also believed to be responsible for the formation of graphitic soot, the high degree of atomic hydrogen production under the high flame temperature with the resonant excitation also eliminated the accumulation of graphitic carbon content through an etching process and ensured a high diamond quality.

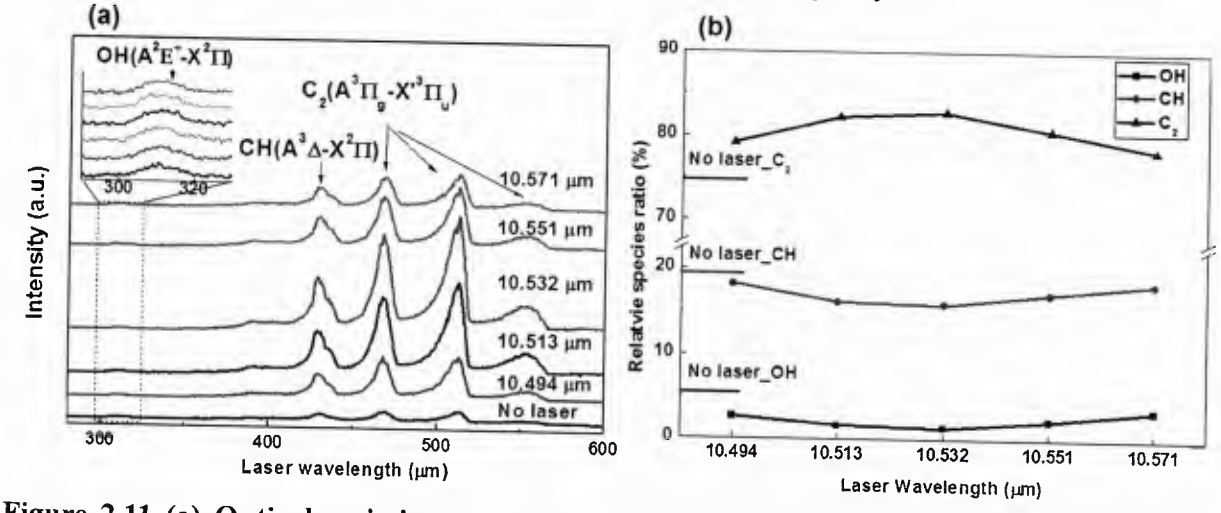

Figure 2.11 (a) Optical emission spectra of $C_2H_4/C_2H_2/O_2$ flames without and with laser excitations at different wavelengths; the inset shows the OH emission line. (b) The relative species concentrations plotted as a function of laser wavelengths.

To understand the effects of laser excitations on the combustion diamond deposition process, the positive charged species concentrations in the $C_2H_4/C_2H_2/O_2$ combustion flames under laser irradiations at different laser wavelengths were studied using MS. **Figure 2.12**(a) shows a typical positive ion mass spectrum of the combustion flames without laser irradiation. Three major types of ions were detected: H_3O^+, $C_xH_y^+$ and $C_xH_yO^+$. H_3O^+ is generated by attaching an H^+ onto a H_2O molecule, which is known as an effective etchant of diamond.[10] C_xH_y+ are important intermediates during the combustion processes as the carbon source for diamond formation. The amount of $C_xH_yO^+$ was far less than that of $C_xH_y^+$. **Figure 2.12**(b) shows the relative concentration profiles of the intermediates as functions of the laser wavelength. The relative concentration of $C_xH_y^+$ (**Figure 2.12**(a)) reached a maximum point (13.0%) at 10.532 μm whereas H_3O^+ (**Figure 2.12**(a)) was in minimum (9.8%) at 10.532 μm. The concentration of $C_xH_yO^+$ was almost constant. The species concentration variations with regard to laser wavelength were attributed to the modified combustion processes under laser excitations. $C_xH_y^+$ species play positive roles in promoting diamond formation via providing the carbon source.[11] The maximum $C_xH_y^+$ concentration under the resonant vibrational excitation indicates that the flame chemistry was modulated to favor the diamond formation. The relatively low

concentration of H_3O^+ under the resonant excitation at 10.532 μm suggests that the flame chemistry was modified in a way that suppressed the diamond etching by water vapor, promising a fast deposition rate. The variation of the flame chemistry with laser excitation demonstrates that the capability of resonant vibrational excitations in modulating the chemical species distribution in a way that facilitated diamond synthesis.

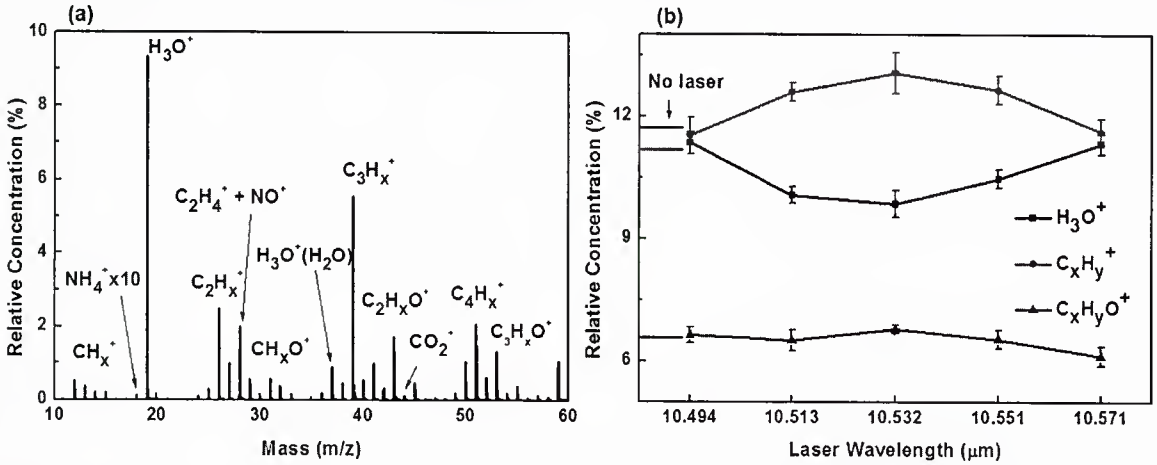

Figure 2.12 (a) A typical positive ion mass spectrum of the combustion flame without laser irradiation. (b)Relative concentrations of positive ions in the flames plotted as a function of laser wavelengths. The color-coded solid bars indicate the relative concentrations of the corresponding species without laser irradiation.

In summary, vibrational excitations of C_2H_4 molecules were studied using a wavelength-tunable CO_2 laser in a combustion CVD process of diamond films. The IR-laser on-resonance excitation at a wavelength of 10.532 μm is more efficient than the off-resonance excitations in exciting the C_2H_4 molecules, elevating the flame temperature, enhancing the deposition rate and improving the diamond quality. The flame variation and the calculated CH rotational temperature with respect to laser wavelengths reveal that the resonant excitation of the CH_2-wagging mode modified the combustion processes in a way that increased the flame temperature. A highly elevated flame temperature under the on-resonance laser excitation at 10.532 μm led to the observed improvement of diamond deposition. Besides the conventional thermal heating effect, the resonant excitation of the precursor molecules influenced the combustion processes in a way that accelerated the reaction rates and modified the flame chemistry. The increase in the C_2 relative concentration and high flame temperature with the resonant laser excitation could explain the enhanced deposition rate and the improved diamond quality. The variation of charged species concentrations upon the laser wavelengths demonstrates that the vibrational resonant excitations modified the flame chemistry in a way that favored the diamond formation.

III. Controlled growth of {100}-textured diamond films using laser-assisted combustion flames

i. Experimental details

The experimental setup and details for crystallography-controlled growth of {100}-oriented diamond deposition using the $C_2H_4/C_2H_2/O_2$ combustion flame are similar to description in Section II, except for different CO_2 laser wavelengths applied. A ro-vibrational transition line of

the CH_2-wagging mode matches one CO_2 laser emission line, 10.22 μm. Diamond depositions were performed with CO_2 laser irradiations at five laser wavelengths centered at 10.22 μm, including 10.195, 10.207, 10.22, 10.233, and 10.247 μm. Surface morphologies of the diamond films were characterized by a scanning electron microscope (SEM; XL-30, Philips Electronics). Diamond qualities were evaluated using a micro-Raman spectrometer (inVia, Renishaw). Diamond film thicknesses were measured using a stylus surface profiler (XP-2, AMBiOS) with a stepping speed of 0.05 mm/s.

ii. Results and discussion

Figure 3.1 shows the CO_2 laser energy absorption spectrum of the $C_2H_4/C_2H_2/O_2$ flame. The predominant absorption peak at 10.22 μm is attributed to a strong resonance to the ro-vibrational sub-band head ($Q^R_{K=3}$, 978.94 cm^{-1}) of the ν_7 mode. As the laser wavelength tuned from 10.22 to 10.182 μm (10.26 μm), the excitation became off resonance and the absorption dropped from 5.52% to 1.41% (0.88%). The decreasing absorptions at off-resonance wavelengths were caused by smaller absorption cross sections.

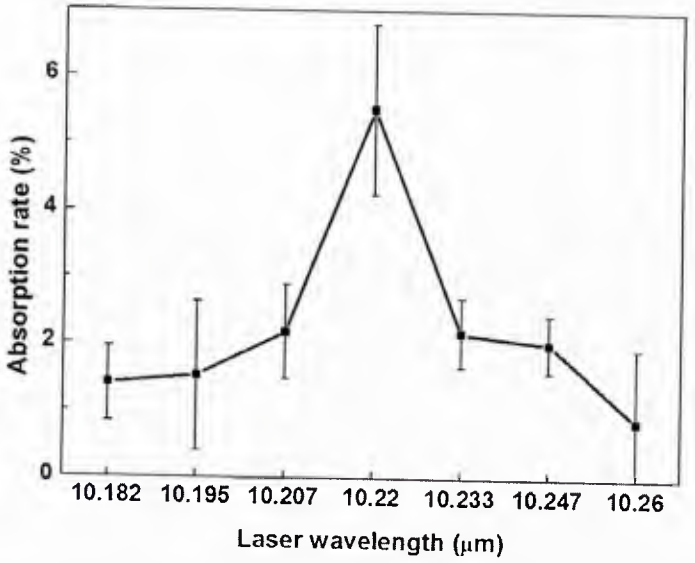

Figure 3.1 CO_2 laser energy absorption spectrum by $C_2H_4/C_2H_2/O_2$ flames, ranging from 10.182 to 10.26 μm.

Figure 3.2 shows optical images of the $C_2H_4/C_2H_2/O_2$ flame without and with laser irradiations at laser wavelengths centered at 10.22 μm. The length of the inner flame was about 5.00 mm without laser irradiation. When a CO_2 laser beam irradiates the flame, the inner flame became brighter and shorter. At 10.22 μm, the inner flame length was the shortest, 4 mm, with 21% expansion in diameter, indicating accelerated combustion processes induced by the laser resonant ro-vibrational excitations. As the laser wavelength was gradually tuned off resonance, the flame bounced back with increased lengths and expanded diameters.

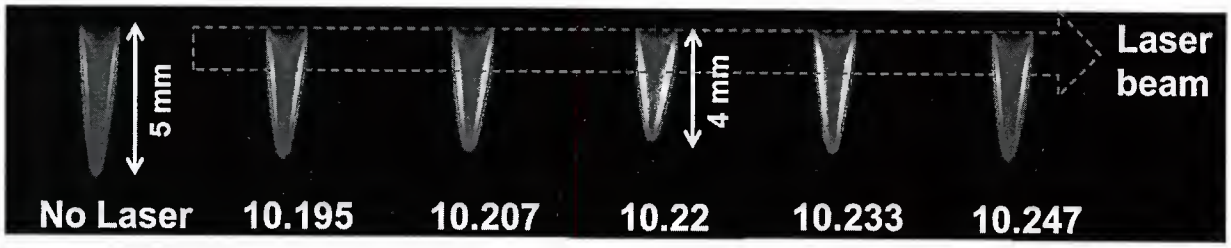

Figure 3.2 Optical images of the $C_2H_4/C_2H_2/O_2$ flames without and with laser irradiations at laser wavelengths of 10.195, 10.207, 10.22, 10.233, and 10.247 μm.

The diamond film morphologies are shown in **Figure 3.3**. Diamond films deposited without laser irradiation consisted of randomly oriented grains with an average grain size of 2.6 μm (**Figure 3.3**(a)). {100}-oriented facets were observed in the center areas of the diamond films deposited with laser excitations at 10.195 μm (**Figure 3.3**(b)). The preferential growth of {100}-oriented facets with an average size of 6 μm became more dominant at 10.207 μm (**Figure 3.3**(c)). With on-resonance excitation at 10.22 μm, {100}-oriented grains were uniformly distributed in the center area of diamond films (**Figure 3.3**(d)). The orientations of the diamond facets became randomly distributed as the laser wavelengths was further tuned from 10.233 to 10.247 μm, as indicated in **Figure 3.3**(e) and (f). The diamond grain size increased as laser wavelength approached 10.22 μm, suggesting a faster growth rate.

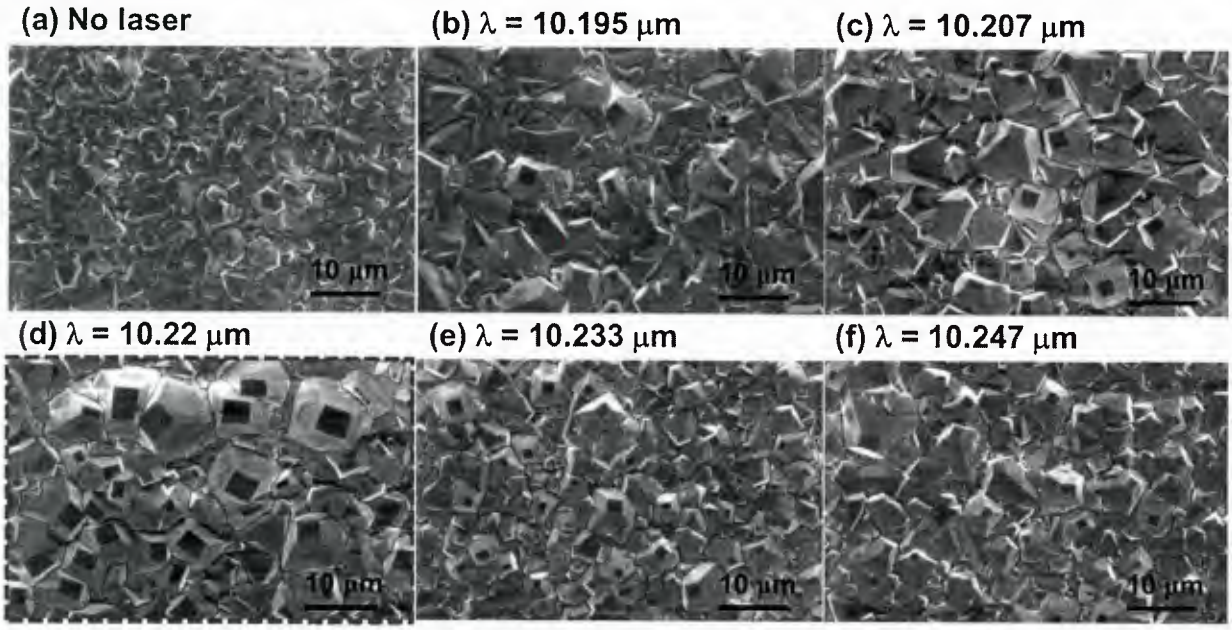

Figure 3.3 SEM micrographs of the center area in diamond films deposited (a) without and with laser excitations at laser wavelengths of (b) 10.195, (c) 10.207, (d) 10.22, (e) 10.233, and (f) 10.247 μm.

The {100}-oriented grains located in the center area of the diamond films and covered an area of 4 mm^2. The average {100}-oriented grain density, μ, is calculated via averaging the density of {100}-oriented diamond grains counted in 5 randomly-selected 60×50 μm^2 areas within the 4 mm^2 interest area via Eq. 3.1:

$$\mu = \frac{\sum N_{100}}{5}. \tag{3.1}$$

The {100}-facet coverage rate, p, is calculated via dividing the sum of {100}-facet covered areas by the view area and averaging over 5 randomly-selected 60×50 μm^2 areas within the 4 mm^2 interest area via Eq. 3.2:

$$p = (\sum \pi \cdot {d_{100}}^2/4) \cdot \mu. \tag{3.2}$$

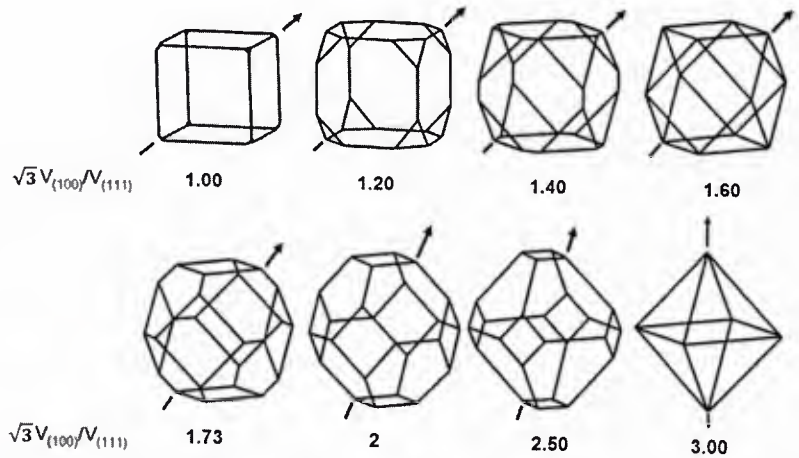

Figure 3.4 Crystal shapes from cubic to octahedral as a function of growth parameters, α. The arrows indicate the fastest growth directions.

The {100}-oriented grain densities and the {100}-facet coverage rates are plotted as a function of laser wavelengths in **Figure 3.5**(a). The sample prepared without laser irradiation had a {100}-oriented grain density of 0.07 per 10×10 μm^2. With laser irradiation at 10.195 μm, the {100}-oriented grain density was 0.93 per 10×10 μm^2, 13 times that without laser irradiation. As the laser wavelength was tuned from 10.207 through 10.22 to 10.233 μm, the {100}-oriented grain densities were 1.60, 1.77 and 1.76 per 10×10 μm^2, respectively. The grain density is directly related to the nucleation stage. Higher nucleation rates leads to higher grain densities. Subtle variance was found in term of the {100}-oriented grain density from 10.207 to 10.233 μm, suggesting the controlled {100}-oriented diamond nucleation reached a stable stage as laser wavelengths turned from 10.207 to 10.233 μm. Meanwhile, the {100}-facet coverage rate with on-resonance excitation at 10.22 μm reached a maximum value, 21.09%, which corresponds to a crystal habit with growth parameter of α = 1.73 ~ 2 as shown in **Figure 3.4**.[5] The high {100}-facet coverage rate at 10.22 μm was attributed to a higher deposition rate. The deposition rates are calculated via dividing the film thicknesses by the deposition time and plotted as a function of laser wavelengths in **Figure 3.5**(b). The deposition rate without laser irradiation was 7.2 μm and reached a maximum value, 26.6 μm/hr, at 10.22 μm. On-resonance ro-vibrational excitation promoted the deposition rate by a factor of 3.5. The deposition rate dropped from 26.4 to 13.1 (14.8) μm/hr as the laser wavelength was tuned off resonance from 10.22 to 10.195 (10.247) μm. The fastest deposition rate with on-resonance ro-vibrational irradiation at 10.22 μm demonstrates the capability of laser resonant excitations in promoting the diamond growth.

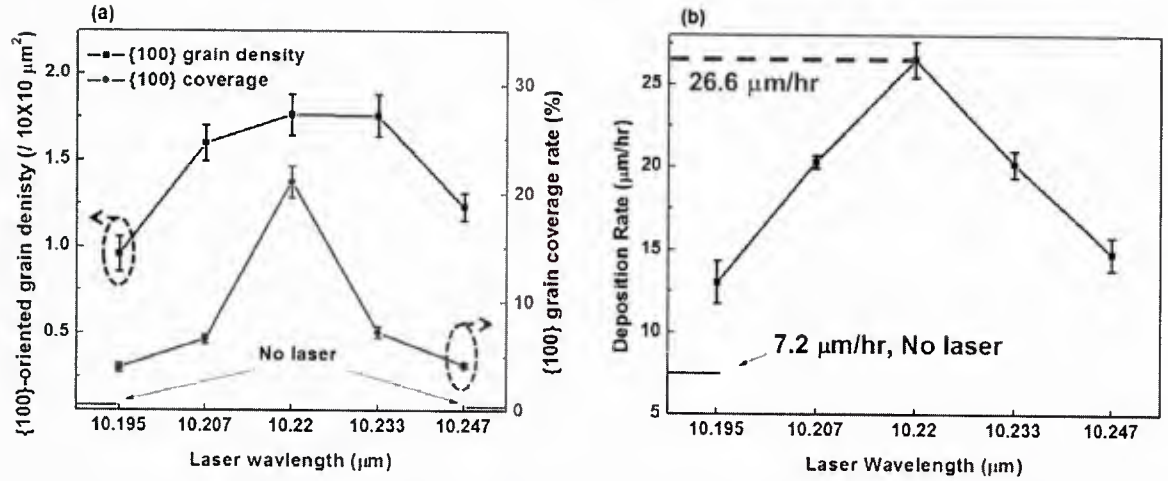

Figure 3.5 (a) {100}-oriented grain densities (black squares) and {100}-facet coverage rates (red circles) plotted as a function of laser wavelengths; (b) deposition rates plotted as a function of laser wavelengths.

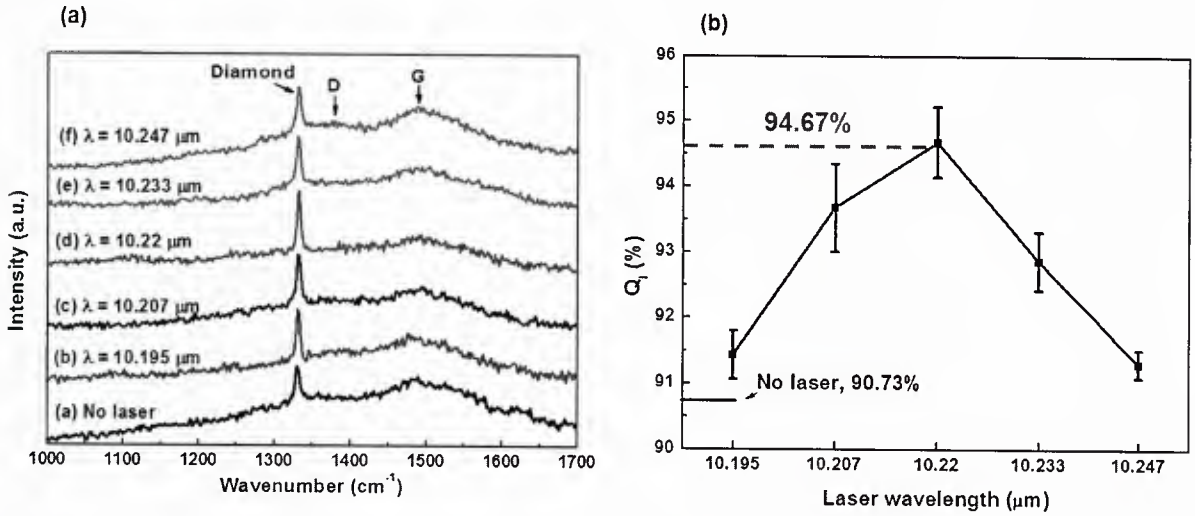

Figure 3.6 (a) Raman spectra of diamond films deposited using $C_2H_4/C_2H_2/O_2$ flames without and with CO_2 laser excitations at different laser wavelengths; (b) Diamond quality index factors of the diamond films plotted as a function of laser wavelengths.

The bonding structures in the diamond films were characterized using Raman spectroscopy as shown in **Figure 3.6**(a). The sample deposited without laser excitation exhibited a strong G-band (centered at 1580 cm^{-1}), a relatively weak diamond peak (1332 cm^{-1}) and a D-band on the shoulder of the diamond peak (1350 cm^{-1}) (see Spectrum (a)). The D- and G- bands relate with non-diamond carbon phase in the diamond matrix. The diamond peak became stronger while the D- and G-band intensities dropped with laser irradiation. The diamond film deposited with laser on-resonance excitation at 10.22 μm showed the sharpest diamond peak associated with the lowest D- and G-band intensities. As the laser wavelength was tuned off resonance to 10.195 (10.247) μm, the diamond peak weakened while the D- and G-bands rose up. The diamond quality index factors were retrieved from the Raman spectra and plotted as a function of laser wavelengths in **Figure 3.6**(b), which exhibited a similar trend to the deposition rate curve shown

in **Figure 3.5**(b). The diamond film deposited with the laser on-resonance ro-vibrational excitation at 10.22 μm had the highest diamond quality factor, 94.67%, which is 3.94% higher than that without laser excitation. High-quality diamond films grown with on-resonance laser excitation at 10.22 μm show the advantages of the laser resonant excitations.

In summary, we have demonstrated that the laser on-resonance excitation of ro-vibrational sub-band head of v_7 mode of C_2H_4 molecules was efficient in controlling the crystallographic orientation in combustion CVD of diamond films. With on-resonance excitation at a laser wavelength of 10.22 μm: the {100}-facet coverage rate reached a peak value of 21.09%, the deposition rate was enhanced by a factor of 3.5, and the diamond quality factor increased by 3.94%. The {100}-oriented diamond growth, the enhancement in deposition rate and improvement in diamond quality became less pronounced as the laser wavelength was tuned off resonance. The brightest and shortest flame under on-resonance ro-vibrational excitations suggests that the diamond deposition was modified in a way that increased the flame temperature, which is beneficial for diamond formation.

IV. Synthesis of N-doped diamond films using combustion flames with vibrational excitations of ammonia molecules

i. Experimental details

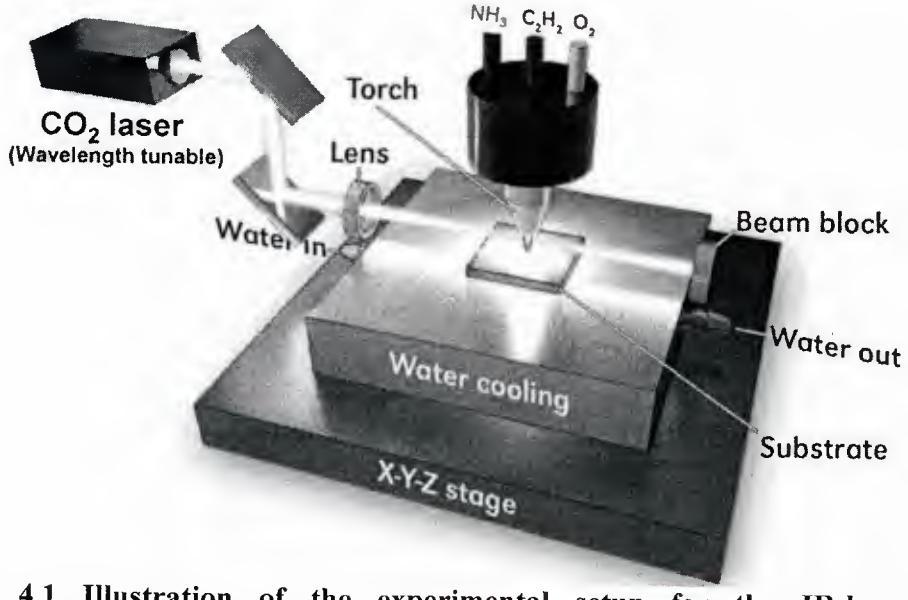

Figure 4.1 Illustration of the experimental setup for the IR-laser-assisted combustion flame method for nitrogen-doped diamond deposition in open air.

The experiment system for the CO_2 laser-assisted combustion for N-doped diamond deposition is similar to that used in previous chapter, as illustrated in **Figure 4.1**. A commercial oxy-acetylene torch with a 1.5-mm orifice tip was used to generate oxyacetylene flames. Acetylene (C_2H_2, 99.6%), oxygen (O_2, 99.996%), and ammonia (NH_3, 99.99%) gases were mixed in a torch through three gas-flow meters (B7920V, Spec-Air Gases & Technologies). The NH_3 gas acted as a N source and the absorption medium of CO_2 laser energy via laser-induced vibrational excitations. The gas flow rates of C_2H_2, O_2, and NH_3 were 1.2, 1.18, and 0.15 standard liters per

minute (slm), respectively. A wavelength-tunable CO_2 laser (PRC, spectrum range from 9.2 to 10.9 μm) was used in the synthesis process. Wavelengths of 9.219, 10.35, 10.719 μm (matching the vibrational transitions of the N-H wagging mode, U_2), and 10.591 μm (wavelength from common commercial CO_2 lasers) were used in this study. The incident laser power was adjusted to have 20 W of CO_2 laser power absorbed by the combustion flame at all the laser wavelengths. The original laser beam has a diameter of around 13 mm. For a comparison, an NH_3-free flame with the same gas flows of oxygen and acetylene was investigated. A deposition time of 30 min was used for all experiments.

An absorption spectrum of NH_3 was obtained in a vacuum chamber with a diameter of 40.64 cm at an NH_3 gas pressure of 12.1±0.2 Torr. A power meter was used to measure the laser power before and after the laser beam passed through the chamber. The CO_2 laser energy absorption spectrum of the NH_3 gas was measured within a spectral range from 9.2 to 10.9 μm.

ii. Results and discussion

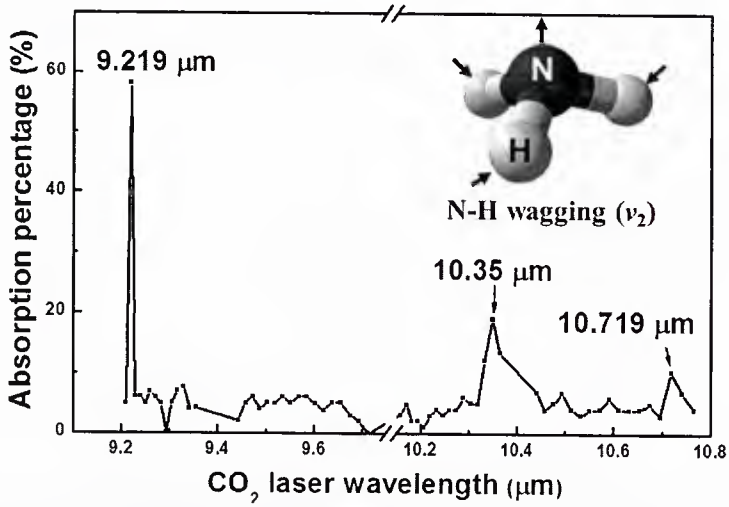

Figure 4.2 A CO_2 laser energy absorption spectrum by NH_3 gas at room temperature. The inset is a schematic illustration of the NH-wagging mode (v_2) of NH_3.

Figure 4.2 shows a CO_2 laser energy absorption spectrum of NH_3 gas within a spectral range from 9.2 to 10.9 μm. Absorption coefficients, α, are determined from the equation $T = \exp(-\alpha u)$; u is the absorber thickness given by pl, where p is the partial pressure of the NH_3 gas and l is the path length. Three distinct absorption peaks were found at 9.219, 10.35 and 10.719 μm, which all are all attributed to the NH wagging mode of NH_3 molecules. Among the six vibrational modes of the NH_3 molecules, the NH-wagging mode (v_2) has a strong IR activity within the CO_2 laser spectrum range. Inset of **Figure 4.2** schematically illustrates the NH-wagging mode. An NH_3 molecule vibrates in an umbrella inversion way in its NH-wagging mode.[12] Due to the barrier that the nitrogen encountered on its travel through the proton plane, the vibrational level splits into two components level at 932.51 cm^{-1} (v_2+) and 968.32 cm^{-1} (v_2−), respectively.[12] Under wavelength-matched laser irradiations, the NH-wagging vibration mode is significantly accelerated and NH_3 molecules are pumped up to excited states. The strongest absorption peak at 9.219 μm (equivalent to 1084.71 cm^{-1}, α = 4.12 $atm^{-1}cm^{-1}$) corresponds to the ro-vibrational transition at 1084.63 cm^{-1} [5(J) → 6(J′), K = 0] in the v_2− band.[12] The excellent match between

the laser emission line (1084.71 cm^{-1}) and the centers of the NH_3 absorption lines (1084.63 cm^{-1}) yields a high absorption cross section at 9.219 μm. Two weaker peaks at 10.35 μm (equivalent to 966.18 cm^{-1}, α = 0.99 $atm^{-1}cm^{-1}$) and 10.719 μm (equivalent to 932.93 cm^{-1}, α = 0.51 $atm^{-1}cm^{-1}$) arise from the Q-branch at 965.99 cm^{-1} (J = K = 5) in the v_2- band and the Q-branch at 932.40 cm^{-1} (J = K = 2) in the v_2+ band, respectively. The considerable mismatch, 0.5 cm^{-1}, between the laser line and the transition line of NH_3 diminishes the absorption efficiency at the latter two wavelengths. No obvious absorption was found at 10.591 μm which is a common wavelength of commercial CO_2 lasers.

Figure 4.3 shows optical images of the combustion flame without and with laser irradiation at different wavelengths. Although the environment condition in pure NH_3 gas at room temperature is different from that in flames, an intensive shrink of the flame image observed with the laser excitation at 9.219 μm indicates a high-efficiency laser energy coupling. Original length of the NH_3-added oxyacetylene flame inner cone without laser irradiation was around 3.5 mm. With laser irradiation at a laser wavelength of 10.591 μm, which is non-resonance with the NH-wagging mode, the flame slightly shrank to 3.3 mm associated with a brightened center in the inner flame. As changing the laser wavelength to 10.35 and 10.719 μm, at which vibrational excitations of NH_3 were achieved but with absorption rates less than 1/3 of that at 9.219 μm, the flame length shrank further and became brighter. With a laser irradiation at 9.219 μm, the flame length was the shortest, 2.3 mm, associated with a 15% expansion in diameter. The shrink of the flame was due to the highly accelerated combustion reactions in the flames induced by the resonant excitations of NH_3 molecules. The shortest and brightest flame with the laser vibrational excitation at 9.219 μm suggests that the resonant vibrational excitations influenced the flame in a way that accelerated the combustion reactions. Without NH_3 addition, a pure oxyacetylene flame had neither laser absorption nor visible change in the flame size with the laser irradiation at all the wavelengths.

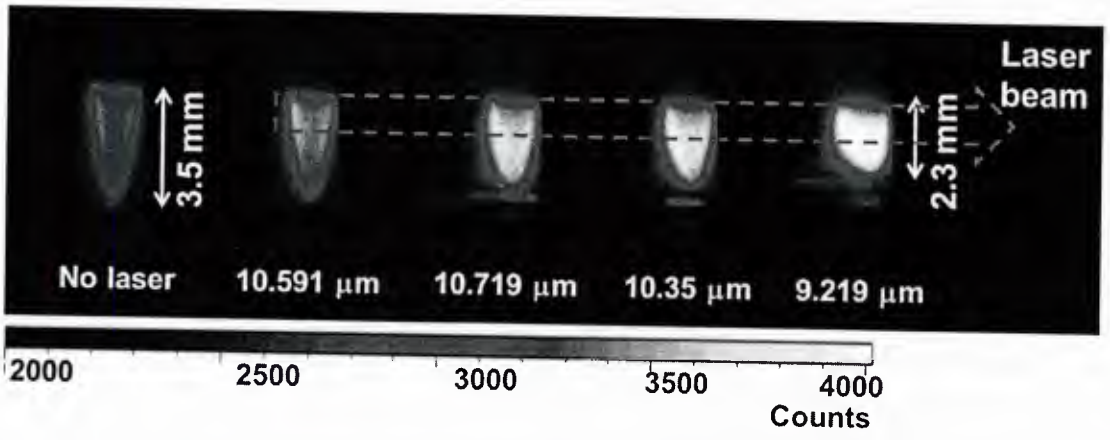

Figure 4.3 Optical images of ammonia-added oxyacetylene flames without and with laser irradiation at different laser wavelengths.

Figure 4.4 shows the SEM images of the deposited films. Uniform and clear diamond films were steadily obtained using a pure oxyacetylene flame with an oxygen to acetylene ratio of about 1:1 (**Figure 4.4**(a)). The film deposited using NH_3-added flames without laser excitations had

amorphous cauliflower-like structures as shown in **Figure 4.4**(b). The morphological change observed upon NH_3 addition agrees with the results obtained by other techniques.[13] Substantial N-containing additive in the diamond deposition process considerably reduced diamond quality and led to preferential sp^2 carbon deposition. With a laser irradiation at 10.591 μm, similar cauliflower-like structures were observed in the deposited film (**Figure 4.4**(c)). In the film deposited at 10.719 μm (**Figure 4.4**(d)), spherules consisting of poorly faceted diamond grains were observed. The ball-like structures became indistinguishable in the film deposited with laser excitation at a wavelength of 10.35 μm (**Figure 4.4**(e)). Clear diamond grains with an average size of 2 μm were observed in the film. With a laser excitation at the strongest absorption wavelength, 9.219 μm, (111)-facet diamond grains with an average diameter of 5 μm were clearly observed (**Figure 4.4**(f)). A high N doping concentration, 1.5×10^{20} atom/cm^3, was determined for the sample prepared with laser excitation at 9.219 μm. Such a high level doping is believed to be difficult to achieve when using nitrogen or NH_3 as dopant sources.

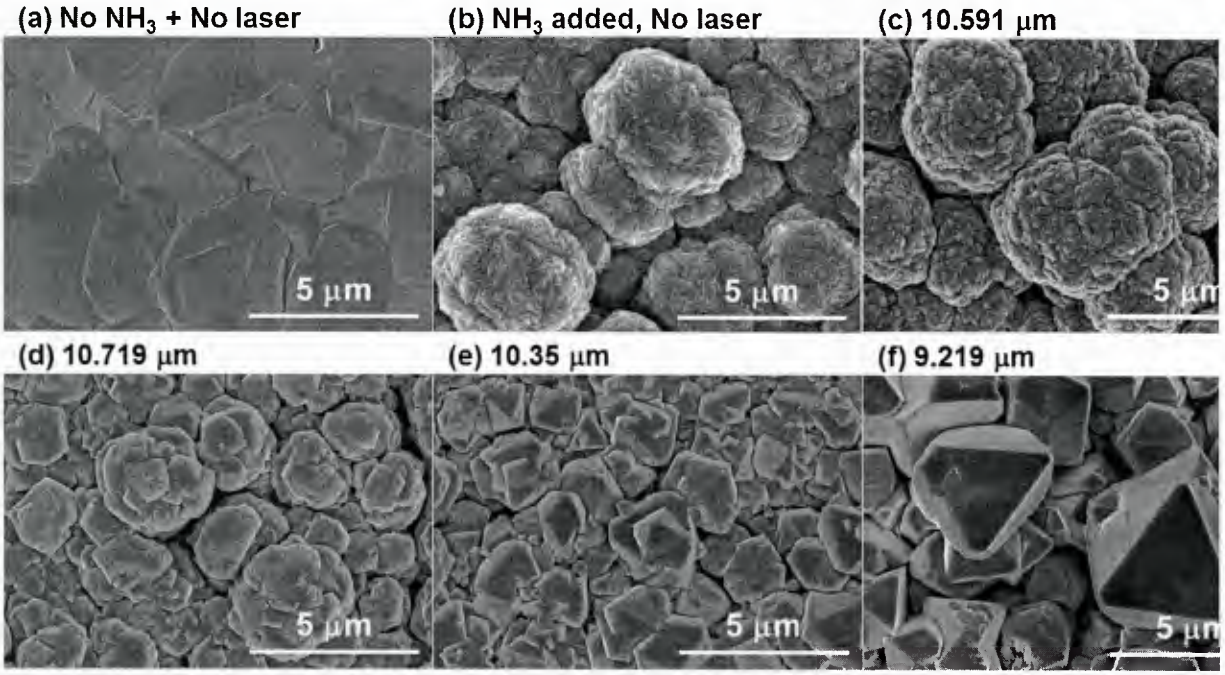

Figure 4.4 SEM micrographs of the diamond films deposited using ammonia-free flames (a), and ammonia-added flames without laser (b) and with 500 W CO_2 laser excitations at 10.591, 10.719, 10.35, and 9.219 μm (c-f).

The bonding structures in the diamond films were characterized by Raman spectroscopy as shown in **Figure 4.5**(a). For all the samples, three carbon-related Raman peaks are resolved: a sharp diamond peak at 1332 cm^{-1}, a D-band on the shoulder of the diamond peak centered at 1350 cm^{-1} and a broad G-band centered at 1550 cm^{-1}. The D-band is attributed to the breathing modes of sp^2 atoms in rings, reflecting disordered carbon in the film. The broad G-band is attributed to the bond stretching of all pairs of sp^2 atoms in both rings and chains and indicates graphite-like carbon content mixed with amorphous carbon. Quality index factors, Q_i, are calculated from the Raman spectra. The Raman spectrum of the film deposited using NH_3-free flames had a sharp and intensive diamond peak at 1332 cm^{-1} associated with a small G-band at 1550 cm^{-1}. The high Q_i value, 97.81%, of the film indicates a pure diamond phase and high

diamond quality. The Raman spectrum of the film deposited using NH_3-added flames without laser excitation possessed a typical nanocrystalline diamond feature with a Q_i value of 86.28%, as shown in spectrum (a). Two extra peaks at 1170 and 1493 cm^{-1} were also resolved for the sample. The peaks at 1170 and 1493 cm^{-1} are signatures of trans-polyacetylene which is related to the hydrogen content in the nanodiamond lattices. The film deposited under the laser excitation at 10.591 μm had a similar nanocrystalline diamond Raman feature. At 10.35 and 10.719 μm, the diamond peaks in spectra (c) and (d) obviously increased associated with continuously weakened D- and G-bands. For the film deposited at 9.219 μm, the diamond peak was the sharpest and strongest associated with the weakest D and G bands, suggesting an improvement in the diamond quality. The quality factor, 90.03%, is around 4% higher than that of the film deposited without laser excitations. The diamond quality index factors (Q_i) of the diamond films prepared under different conditions are shown in **Figure 4.5**(b). Compared with the diamond films prepared without or with laser irradiation at a non-resonance wavelength of 10.591 μm, laser resonant excitation showed the advantage in promoting the diamond quality. The diamond quality factor increased as the excitation became stronger. High-quality N-doped diamond films grown with resonant laser excitation at 9.219 μm showed the advantage of vibrational resonant excitations on reaction control.

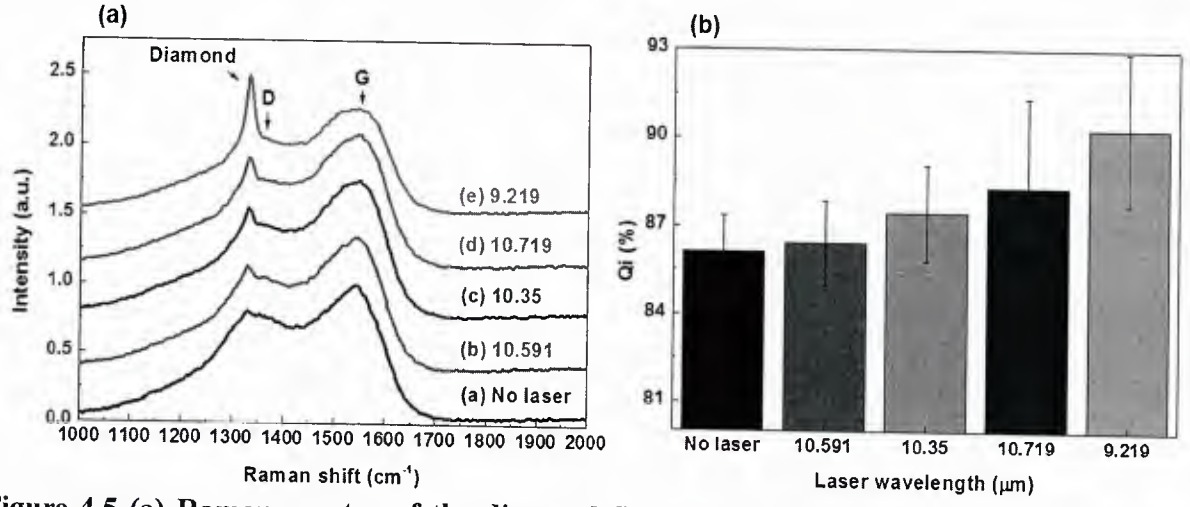

Figure 4.5 (a) Raman spectra of the diamond films deposited using ammonia-free flames (a) and using ammonia-added flames without and with laser irradiation at different laser wavelengths. (b)Diamond quality factors, Q_i, of the diamond films prepared under different conditions.

It was demonstrated that the laser resonant excitation of NH_3 molecules resulted in an enhanced reaction rate and an increase in the concentrations of several intermediate species. OES of the flames was conducted to examine the species in the flames as shown in **Figure 4.7**. Compared with the spectra of NH_3-free flames, the NH_3-added flames showed a considerable declination of C_2 and CH radical intensities while an intensive CN peak centered at 380 nm rose up. With laser excitations at 10.591 and 9.219 μm, the intensity of the whole spectra increased by 41.0% and 107.6%, respectively. The enhanced OES spectrum intensity indicates more excited radicles generated in the flame caused by the highly accelerated combustion reaction process with resonant laser excitation.

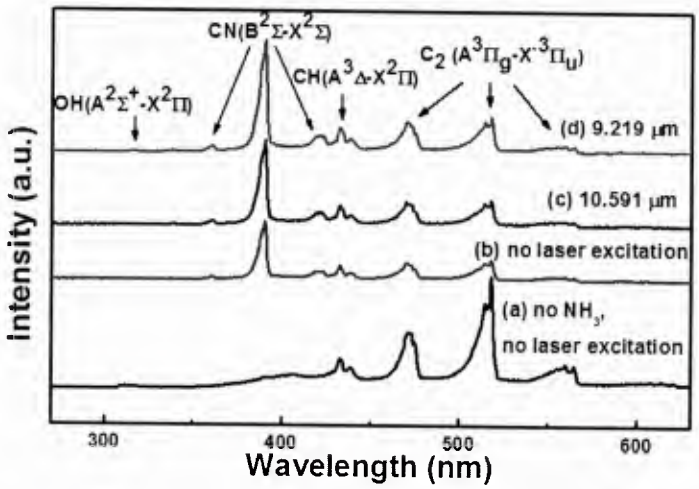

Figure 4.6 Optical emission spectra of ammonia-free oxyacetylene flames (a), and ammonia-added flames with no laser excitation (b) and with 500 W CO_2 laser excitations at 10.591 μm (c) and 9.219 μm (d).

As far as the combustion-flame CVD is concerned, a number of charged chemical intermediates are present in flames. Ionization of intermediates occurs in the combustion flames, making the flames suitable for direct analysis using MS. MS of the flames was carried out to simultaneously detect both positive and negative ions to understand the effect of laser resonant excitation on the gas phase chemistry. The experimental setup for the MS studies is similar to the description in Section I.

Figure 4.8 shows two typical mass spectra obtained for positive (**Figure 4.8**(a)) and negative (**Figure 4.8**(b)) ions in the inner flame tip region of the combustion flame under different conditions. Each line is assigned to an ion in the flames. Due to the increased uncertainties with mass number, only ions in the range of 10 - 60 m/z were investigated.

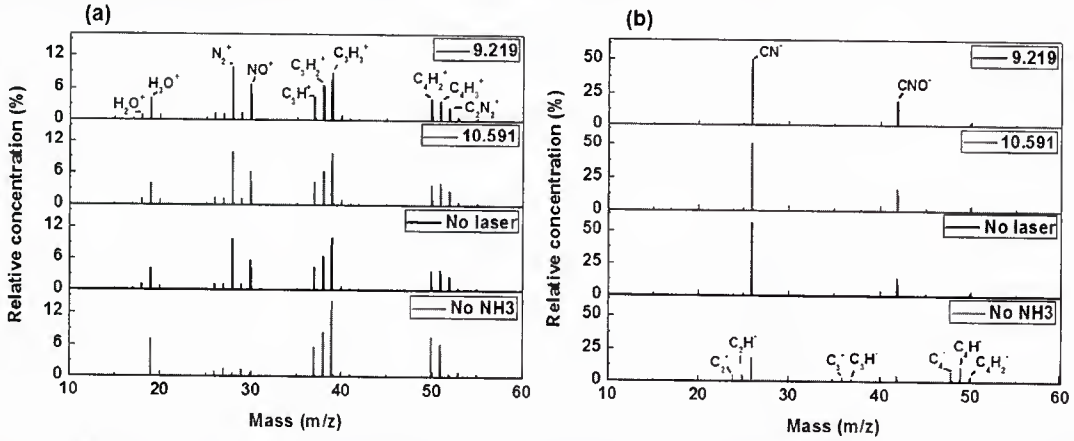

Figure 4.7 Mass spectra of (a) positive and (b) negative ions of the NH_3-free oxy-acetylene flames and NH_3-added oxy-acetylene flame without laser irradiation and with laser irradiation at laser wavelengths: 10.591 and 9.219 μm.

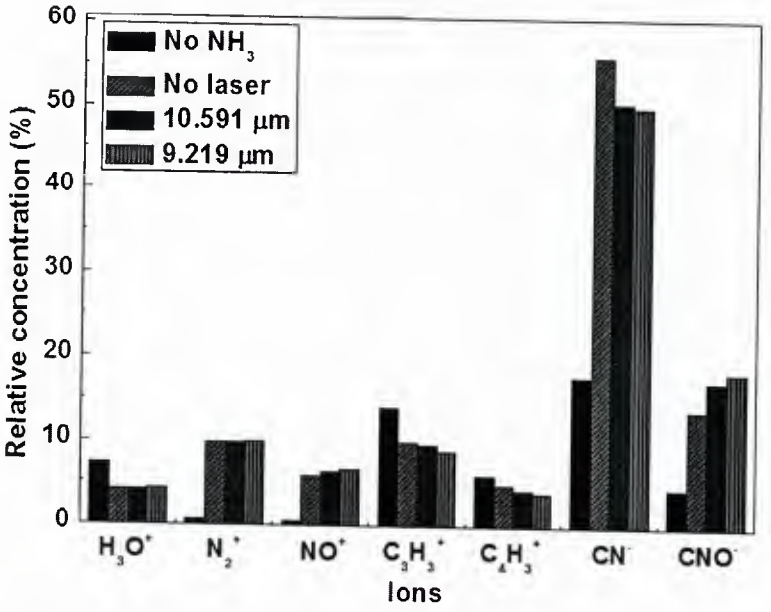

Figure 4.8 Ion relative concentrations in the flames under different experimental conditions.

Both $C_xH_y^+$ (x = 3-4, y = 1-3) and $C_xH_y^-$ (x = 2-4, y = 1-2) ion were dominant in the ion spectra of the ammonia-free flames. H_3O^+ formed by attaching an H atom to a H_2O molecule presented in all positive ion spectra (**Figure 4.8**(a)). As 150 sccm NH_3 was introcuted into the oxyacetylene flame, N-containing ions, including N_2^+, NO^+, $C_2N_2^+$, CN^- and CNO^-, rose up in **Figure 4.8**(a) and (b), whereas the relative concentrations of the hydrocarbon ions reduced (**Figure 4.8**(a) and (b)). To get a more clear view of how the ion relative concentrations varied upon the experimental conditions, the relative concentrations of several key ions are plotted as a function of the experimental conditions in **Figure 4.9**. Compared with the NH_3-free oxy-acetylene flame, the addition of 150 sccm NH_3 led to a more than 3 times increase in the relative concentrations of N-containing ions while $C_xH_y^+$ ion concentrations decreased by at least 25%. Compared with the NH_3-added oxyacetylene flames without laser irradiation, the change of H_3O^+ was subtle with laser irradiation at either 10.591 mm or 9.219 μm. The relative concentration of hydrocarbon ions ($C_3H_3^+$ and $C_3H_4^+$) reduced while a noticeable increase of N-containing ions (N_2^+, NO^+, CNO^-) was observed with laser irradiation at 10.591. The increase of hydrocarbon ions ($C_3H_3^+$ and $C_3H_4^+$) and the decrease of N-containing ions (N_2^+, NO^+, CNO^-) became enhanced with laser resonant excitations at 9.219 μm. The relative concentrations of all N-containing ions were summed up, suggesting a 2.29% increase of the overall N-containing species (N_2^+, NO^+, CN^-, CNO^-). During the course of the reactions in the combustion flame, laser vibrational excitations played an important role by actively intervening in the reaction. The selective excitation of NH_3 molecule steered the gas phase chemistry and resulted in increase in N-containing species. The increase in the N-containing species explains the high doping level in the diamond films deposited at 9.219 μm. A pronounced difference, however, is a smaller CN^- concentration at 9.219 μm compared with that without laser irradiation. It was reported that CN radicals have a two-sided effect on diamond growth.[14] Abstraction of hydrogen from the surface to form HCN or H_2CN promotes diamond growth if a small amount of N-containing species is added. With substantial N-containing additives, the high bond dissociation energy (D_0 = 180

kcal/mol) and the large dimerization energy (ΔH = -134 kcal/mol) of the CN radicals favors the formation of cyanogen (C_2N_2).[14] The condensed paracyanonen could induce the cauliflower structures. This might explain the structure distortion with the NH_3 addition. With resonant laser excitations, the flame chemistry was modified. The increasing etching species (H and OH) under the high flame temperature and the decreasing CN^- relative concentrations suppressed the formation of paracyanonen, contributed to the reproduction of diamond growth sites and promoted micro-crystalline diamond deposition. Diamond deposition became dominant in the competition between diamond and graphite growth. The gas phase chemistry redistribution induced by vibrational excitations of NH_3 molecules demonstrates the advantage of laser excitations in materials synthesis.

In summary, vibrational resonant excitations of NH_3 molecules were achieved using a wavelength-tunable CO_2 laser in combustion CVD of N-doped diamond films. The chemical reaction in the diamond-forming combustion flame was steered by laser resonant excitation of NH_3 molecules. Compared with laser wavelengths of 10.35, 10.719, and 10.591 μm, the laser excitation at 9.219 μm, which corresponds to the strongest absorption peak, was more effective in exciting the NH_3 molecules and promoting the high-quality N-doped diamond deposition. The OES and MS investigations both suggest that the reaction pathway was steered with the resonant laser excitation at 9.219 μm in a way facilitated the N-doped diamond formation. The increase in the N-containing species in the flames with resonant laser excitations explained the high doping level. Suppression of the CN radical generation in the flame with laser resonant excitation of NH_3 played a critical role in the observed morphology transition and micro-crystalline N-doped diamond deposition. Vibrational resonant excitation of precursor molecules was proven to be a promising approach for achieving high-quality N-doped diamond films.

V. Mass spectrometric investigation on the roles of key chemical intermediates in diamond synthesis

i. Experimental details

The experimental setup for the MS studies is schematically shown in **Figure 5.1**. Ionization of intermediates occurs in the combustion flames, making the flames suitable for direct analysis using MS. Combustion flames were produced by a gas mixture of C_2H_4, C_2H_2, and O_2 with flow rates of 35, 35 and 60 - 80 standard cubic centimeters per minute, respectively. Both positive and negative ions in the flames were detected using a time-of-flight mass spectrometer (MS, AccuTOF^{TM}, JEOL USA, Inc.). A stainless steel orifice with an inner diameter of 400 μm was used to collect ions from the flames in open air. The combustion torch was fixed on a motorized 3D stage. The relative position of the flames to the orifice was precisely controlled at a resolution of 2.5 μm. The mass range investigated was from 10 to 60 m/z. The MS data were analyzed using the TSSPro software (Shrader Analytical and Consulting Laboratories, Inc. Version 3.0) and the MS Tools software (JEOL USA, Inc.). An unperturbed $C_2H_4/C_2H_2/O_2$ flame structure is shown in **Figure 5.1**. There are three distinct regions in a flame: (a) inner flame, (a) feather region, and (3) outer diffusion flame. Diamond was obtained within a narrow area in the feather region right below the inner flame tip, which is named as the "tip" region in the following discussion. As an important parameter, the distance from the sampling orifice to the torch nozzle is defined as *h* in the following discussion. A suitable *h*, from 3.1 to 3.5 mm, was required to achieve an effective diamond deposition.

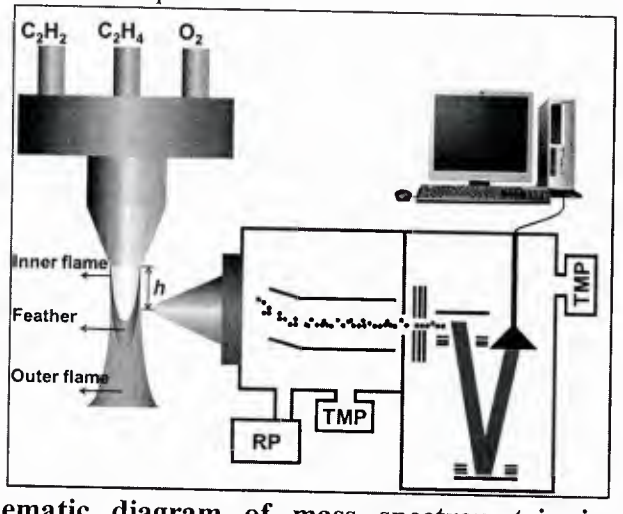

Figure 5.1 A schematic diagram of mass spectrometric investigation of the $C_2H_4/C_2H_2/O_2$ combustion flame.

ii. Results and discussion

In order to understand the diamond formation process, MS investigations on the combustion flames were performed. **Figure 5.2** exhibits two typical mass spectra obtained for positive,

Figure 5.2(a), and negative, **Figure 5.2**(b), ions in the $C_2H_4/C_2H_2/O_2$ flames without laser irradiation at the tip region (h = 3.3 mm), which was an optimized position for diamond deposition. Each line is assigned to an ion in the flames. Ion identification adopted the chemical assignations suggested in Ref [15]. Due to the increased uncertainties with mass number growth, only ions in the range of 10 - 60 m/z were investigated. The relative concentration of each ion was derived by dividing its intensity with the total ion count value in order to eliminate the variation of its absolute value in different measurements.

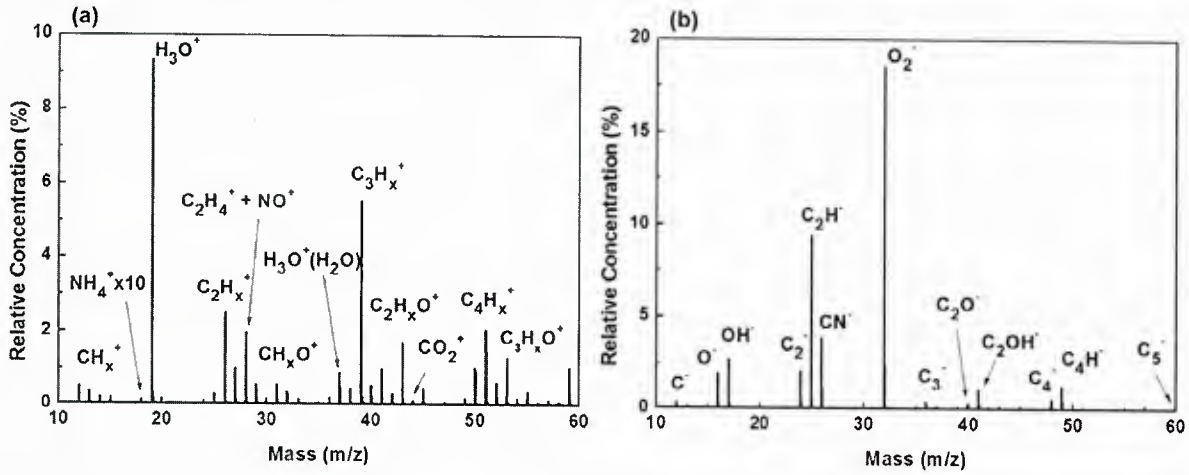

Figure 5.2 Typical mass spectra of positive (a) and negative (b) ions in the combustion flames at the tip region.

The positive ions (**Figure 5.2**(a)) are classified into three categories: diamond etchant (H_3O^+), hydrocarbons ($C_xH_y^+$, x = 1 - 4, y = 1 - 4) and oxygenated hydrocarbons ($C_xH_yO^+$, x = 1 - 3, y = 1 - 3). H_3O^+ ions were the most abundant species in the flames, which were produced by adding a proton to each H_2O molecule, reflecting the formation of neutral H_2O molecules during the combustion process. H_2O was reported to be an effective diamond etchant.[10] The persistence of $C_xH_y^+$ and $C_xH_yO^+$ ions indicates the presence of large quantity of hydrocarbon-related intermediates in the flames. The negative ions (**Figure 5.2**(b)) are categorized in a similar way: carbon etchant (OH^-), carbon cluster and unsaturated hydrocarbons (C_x^- and C_xH^-, x = 1 - 4), and oxygen (O_2^-). The dominant ions, O_2^-, were formed by attaching an electron to an oxygen molecule, which reflected the consumption of oxygen in the gas mixture. Numerous reports have reported that OH^- is critical in combustion synthesis of diamonds by preferentially etching the sp^2-hybridized graphitic carbon and stabilizing the sp^3-hybridized carbon phase.[11] C_x^- and C_xH^- were suggested to be responsible for carbon soot formation in the hydrocarbon flames, which is undesirable in diamond synthesis.[16] The species in each category were found to exhibit similar variation trends with regard to the experimental parameters (h and gas compositions). For a conclusion on the roles of these species for the diamond growth mechanism, it is not sufficient to discuss their concentrations alone. The relative concentrations of the species in each category were therefore added up to obtain an overall variation trend for each category. Other ions, like CO^+, CO_2^+, NH_4^+, CN^- and C_2O^-, were also detected in MS with much lower concentrations. CO^+,

CO_2^+, and C_2O^- are ultimate products of the combustion process and do not exhibit obvious influence in diamond deposition, while NH_4^+ and CN^- are byproducts when reacting with nitrogen in the air.

The diamond deposition is highly sensitive to the distance h and gas compositions. Diamond films were obtained only within a narrow tip region with a hydrocarbon-rich precursor mixture. Experimental parameters, h and the precursor gases ratio, $R = O_2 / (C_2H_2+C_2H_4)$, were varied in diamond growth and MS characterization. The MS results were analyzed in the region: $R = 0.85$ - 1.10 and $h = 2$ - 5 mm.

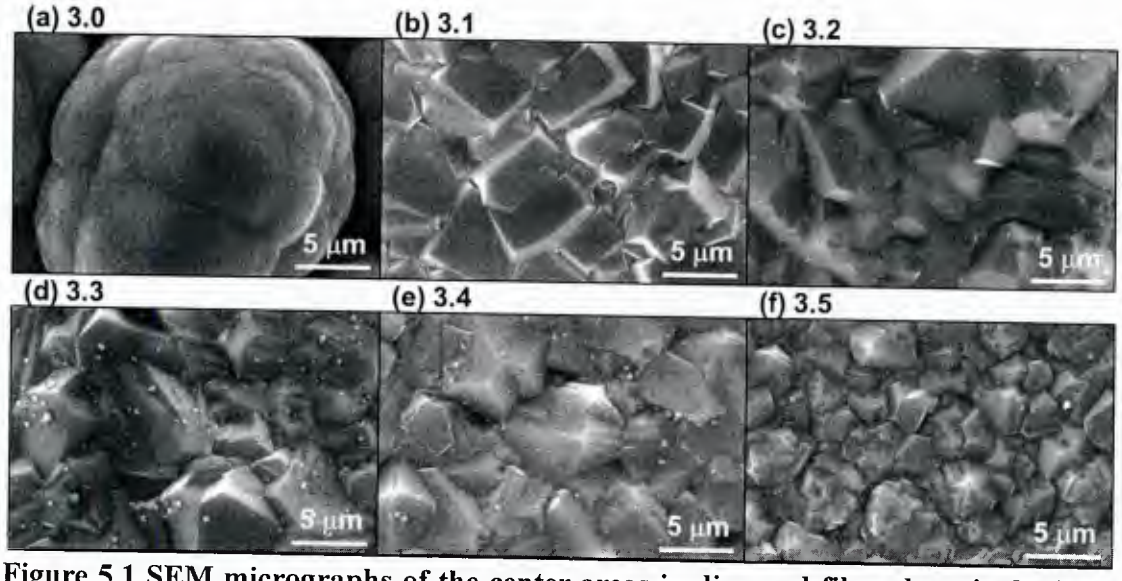

Figure 5.1 SEM micrographs of the center areas in diamond films deposited with a distance *h* from the substrate to the torch nozzle of: (a) 3.0, (b) 3.1, (c) 3.2, (d) 3.3, (e) 3.4, and (f) 3.5 mm.

The distance h between substrates and the torch nozzle played a critical role in diamond deposition. When a substrate was moved from the inner flame through the feather region towards the outer diffusion flame, the carbon deposition channel transited from amorphous carbon to diamond and then to no deposition. **Figure 5.3** shows SEM micrographs of the center areas in diamond films deposited at different h values. With a substrate placed right at the inner flame tip ($h = 3.0$ mm), films with amorphous ball-like structures in the center area were obtained due to fast accumulation of non-diamond carbons (**Figure 5.3**(a)). By moving the substrate downward to $h = 3.1$ mm, {100}-facet diamond grains were observed (see **Figure 5.3**(b)). By further increasing h from 3.2 to 3.5 mm, diamond grains showing random orientations were observed. The grain size decreased with an increasing h value.

The film thicknesses of the diamond films were measured using a stylus profiler. The deposition rates are calculated via dividing the film thicknesses by the deposition time and plotted as a function of h in **Figure 5.4**(a), which exponentially decreased as h increasing from 3.2 to 3.5 mm.

The bonding structures in the diamond films deposited at different h values were characterized using Raman spectroscopy as shown in **Figure 5.4**(b). The Raman peak centered at 1332 cm^{-1} is a typical diamond peak. In the sample deposited at an h value of 3.0 mm, a typical nanocrystalline diamond Raman feature was observed. At an h of 3.1 mm, an intensive diamond peak rose up. As h increases from 3.1 to 3.2 mm, the diamond peak intensity increased and the G-band intensity was suppressed, which indicates an improved diamond quality. With h increased from 3.2 to 3.5 mm, the variation of Raman spectrum feature became subtle. The diamond quality index factors are plotted as a function of h in **Figure 5.4**(a), showing an opposite variation trend to the deposition rates. The diamond quality was drastically improved as the substrate moved from h = 3.0 to h = 3.2 mm and then kept relatively constant with h ranging from 3.2 to 3.5 mm.

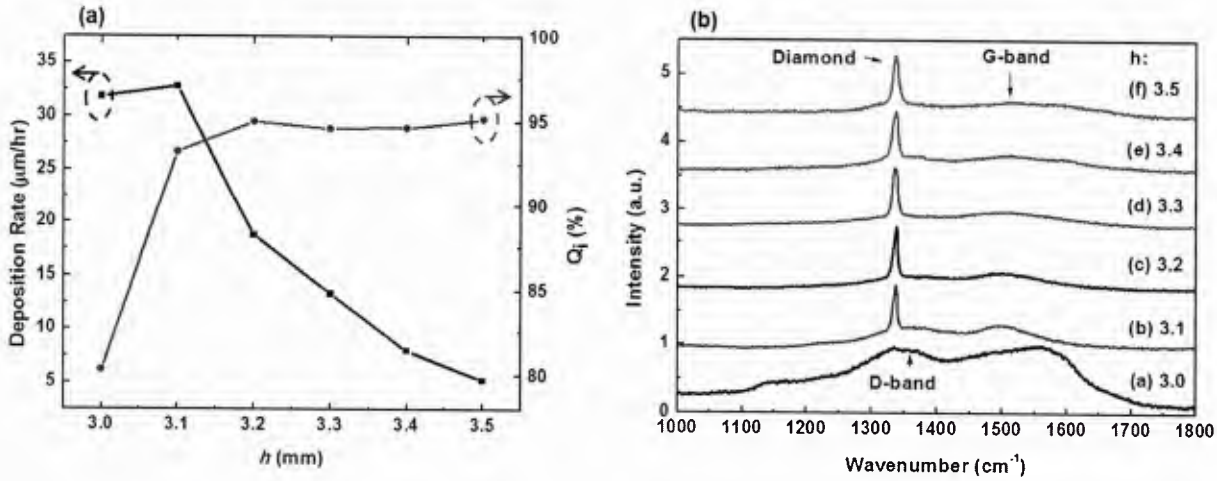

Figure 5.2 (a) Deposition rates (black solid squares) and diamond qualities (red solid circles) plotted as a function of the distance *h*. (b) Raman spectra of center area in diamond films deposited at different distances.

Combustion flames at different h values were studied using MS to investigate the chemical intermediates distribution. The relative concentrations of the positive (H_3O^+, $C_xH_y^+$, and $C_xH_yO^+$) and negative (OH^- and $C_x^- + C_xH^-$) ions in the flames are plotted as a function of h at a gas ratio R = 0.969 in **Figure 5.5**(a) and (b). The gas ratio R = 0.969 was an optimized value for diamond deposition. In the positive ion spectrum (**Figure 5.5**(a)), the relative concentration of H_3O^+ increased from the inner flame zone to the feather zone, reached the maximum in the middle of the feather region, and then fell down in the out diffusion flame. The relative concentrations of $C_xH_y^+$ and $C_xH_yO^+$ kept relative constant in the inner flame, decreased quickly as moving downstream along the feather region and became stable in the outer diffusion flame. The profiles of the positive ions (H_3O^+, $C_xH_y^+$ and $C_xH_yO^+$) in the flames are in good agreement with Hayhurst's observations.

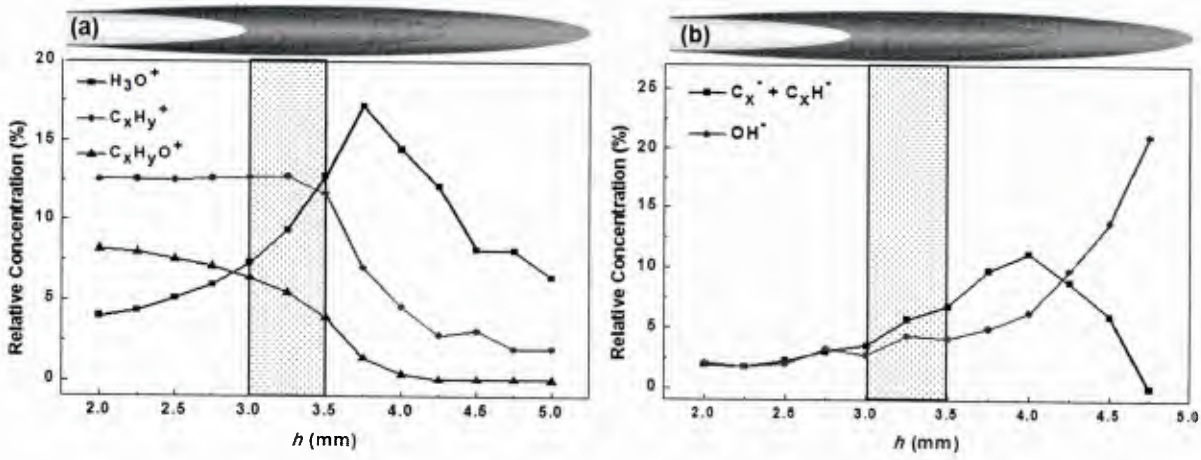

Figure 5.3 Relative concentrations of positive (a) and negative (b) ions in the flames plotted as a function of the distance *h*. The dashed area is the diamond deposition region.

The diamond formation was suggested to be kinetically controlled by the competitive growth of graphite and diamond.[17] Both graphitic carbon (sp^2 hybridized carbon) and diamond carbon (sp^3 hybridized carbon) deposit simultaneously on substrate surfaces, and are etched concurrently by the carbon etchants, e.g. OH^- and H_3O^+. The deposition of diamond films is based on the fact that sp^3-hybridized diamond phase is more stable towards carbon etchants than sp^2-hybridized graphite phase. The carbon etchants play double-bladed roles in the diamond deposition process. With a shortage of etchants, the growth speeds of graphite and diamond are faster than their etching rates, the net result is amorphous carbon deposition. When a moderate amount of etchants present in the gas phase, the etching speed of graphitic carbon is faster than its growth rate while the growth rate of diamond is higher than its etching rate, then the net result is diamond growth. With an existence of excessive etchants, the diamond etching rate exceeds the diamond growth rate and the net result is deteriorated diamond deposition even no carbon deposition at all. The variations of the etching species (H_3O^+ and OH^-) with respect to *h* are therefore particularly interesting, as illustrated in **Figure 5.5**(a) and (b), respectively. The relative concentration of H_3O^+ (**Figure 5.5**(a)) reached a maximum value in the middle of the feather region and then fell down in the outer diffusion flame region. The reduction of the H_3O^+ concentration in the outer diffusion flame is attributed to the electron-H_3O^+ recombination process:[18]

$$H_3O^+ + e^- \rightarrow neurtral\ products. \tag{6.1}$$

The relative concentration of OH^- (**Figure 5.5**(b)) rose up consistently as moving downstream from the inner flame to the outer diffusion flame. When the etchant concentrations (H_3O^+ and OH^-) increased with an increasing *h* from 3.0 to 3.5 mm, the diamond quality (red solid circles in **Figure 5.4**(a)) was drastically enhanced from h = 3.0 to 3.2, then remained relatively constant from h = 3.2 to 3.5, whereas a persistent decrease in diamond deposition rate (black solid squares

in **Figure 5.4**(a)) was observed. This result confirms the positive roles of carbon etchants in diamond synthesis by effectively removing graphitic carbon. It is also noted that further increased etchant concentrations could not improve the diamond quality apparently but led to a fast reduction of the deposition rate due to excessive etching of diamonds.

Hydrocarbon intermediates in the gas-phase reaction were suggested to play active roles in diamond formation as carbon source.[11] As shown in **Figure 5.5**(a), the $C_xH_y^+$ intermediates were abundant in the inner flame. The relative concentration of the $C_xH_y^+$ started to reduce in the tip region, dropped quickly in the feather region, and fell below 2.0% in the out diffusion flame. The decreased $C_xH_y^+$ concentration in the tip region was correlated with a reduction of the diamond deposition rate (black solid squares in **Figure 5.4**(a)). The high relative concentration (11.6 - 13.7%) of hydrocarbon intermediates in the tip region promoted the diamond growth. The relative concentration of $C_xH_yO^+$ exhibited a similar variation trend as the $C_xH_y^+$ but at a much lower concentration.

It is noticed that the relative concentration of C_x^- and C_xH^- increased as moving from the inner flame region to the feather region (**Figure 5.5**(b)). The relative concentration of C_x^- and C_xH^- at the end of the feather region was almost 5 or 6 times higher than that in the inner flame. The high concentration of C_x^- and C_xH^- is attributed to the formation of soot particles at the end of feather region where there was oxygen starvation and the temperature is relatively low.[16]

Another important parameter in combustion diamond synthesis is the oxygen-to-fuel ratio, $R = O_2/(C_2H_2+C_2H_4)$. When $R = 1.0$, a neutral flame is achieved, which is also defined as the condition where the feather region just disappears because all the fuel gases are consumed in the inner flame. The flames with $R > 1$ are called oxygen-rich flames. When $R < 1$, hydrocarbon-rich flames are produced. Y. Hirose *et al.* published a map of diamond growth regimes versus to the O_2/C_2H_2 gas ratio, suggesting that diamond was obtained in a narrow O_2/C_2H_2 ratio range.[19] In this study, diamond films were deposited in the tip region in hydrocarbon-rich flames at an R value ranging from 0.922 to 1.

Figure 5.6 shows the SEM micrographs of diamond films deposited with R ranging from 0.922 to 1 at $h = 3.3$ mm. At $R = 0.922$, amorphous ball-like structures were observed due to graphitic and amorphous carbon accumulation (**Figure 5.6**(a)). At $R = 0.937$, {100}-faceted diamond grains were deposited (**Figure 5.6**(b)). The diamond film morphologies were highly sensitive to the gas phase composition. With R increasing from 0.953 to 1, the diamond grain orientation became random and the grain size decreased due to an insufficient carbon supply and excessive etching in oxidizing conditions (**Figure 5.6**(c)-(f)).

The deposition rates and diamond qualities are plotted as a function of R in **Figure 5.7**(a). The diamond deposition rate reached a maximum value at $R = 0.969$ and experienced a fast reduction with R increasing from 0.969 to 1. The bonding structures in the diamond films deposited as a

function of the gas composition R were characterized using Raman spectroscopy as shown in **Figure 5.7**(b). The diamond obtained at an R value of 0.922 shows a typical nanocrystalline diamond feature. The diamond peak intensity increased with an increasing R value, suggesting an improved diamond quality. The diamond quality index factors are plotted as a function of R in **Figure 5.7**(a). An obvious improvement in term of diamond quality were observed as R increased from 0.922 to 0.953 while it kept relative constant with R higher than 0.953.

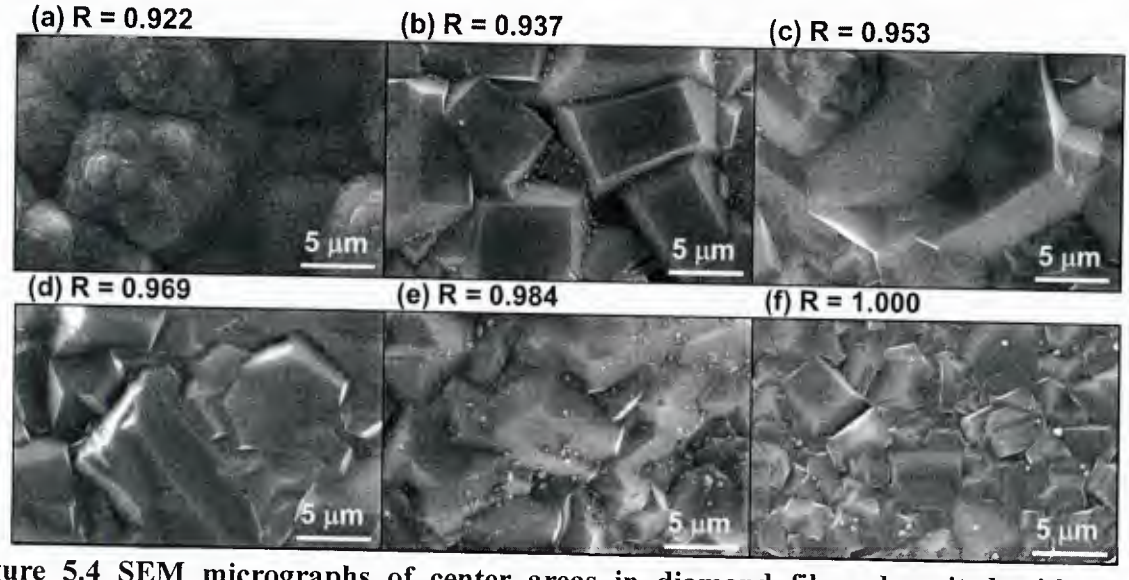

Figure 5.4 SEM micrographs of center areas in diamond films deposited with a gas composition (R) of: (a) 0.922, (b) 0.937, (c) 0.953, (d) 0.969, (e) 0.984, and (f) 1.

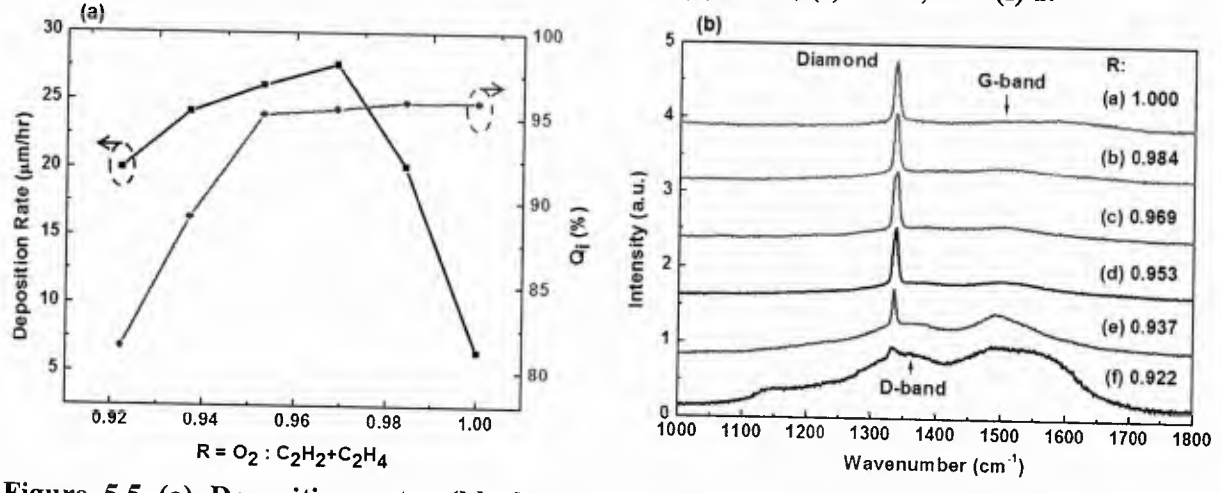

Figure 5.5 (a) Deposition rates (black solid squares) and diamond qualities (red solid circles) plotted as a function of gas ratios, *R*. (b) Raman spectra of center areas in diamond films deposited at different gas ratios, *R*.

The relative concentrations of the positive and negative ions in the flames were plotted as a function of R, at h = 3.3 mm, in **Figure 5.8**(a) and (b), respectively. The relative concentrations of the carbon etchants (H_3O^+ and OH^-) increased constantly from R = 0.92 to 1.0. The

concentration of $C_xH_y^+$ species fell from 13.7% to 13.0% over this narrow range. A concomitant decrease in $C_xH_yO^+$ from 5.5% to 4.9% was also observed. The variation of C_x^- and C_xH^- within the diamond growth region was subtle. The decrease of hydrocarbon-related intermediates and the increase of etchants from hydrocarbon-rich flames ($R < 1.0$) towards oxygen-rich flames ($R > 1.0$) coincided with a growth transition from amorphous carbon to diamond, then to etching of diamond. This result suggests that an appropriate ratio of etchants (H_3O^+ and OH^-) and hydrocarbon-related intermediates ($C_xH_y^+$ and $C_xH_yO^+$) was required to realize diamond formation. A counterbalance between the growth and the etching of diamond and graphitic carbon was required for growing diamond.

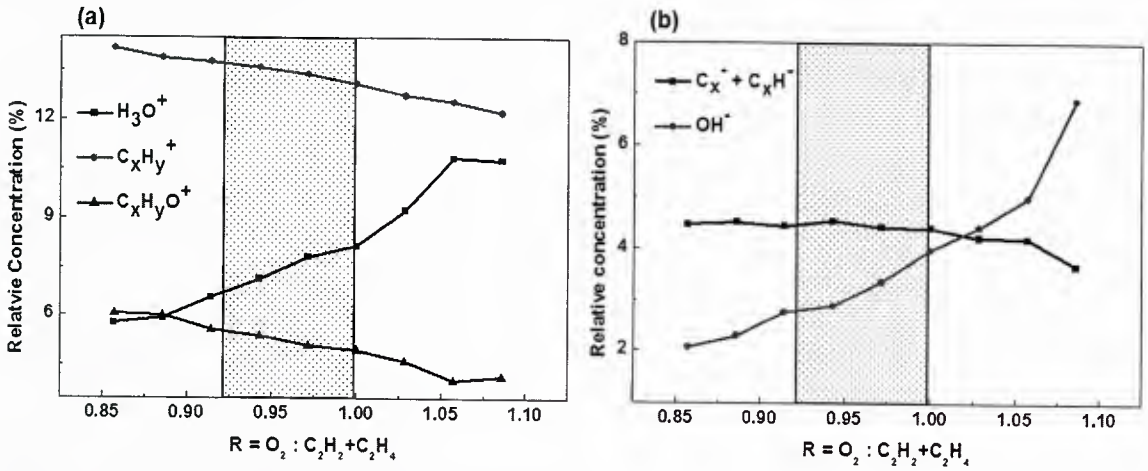

Figure 5.6 Relative concentrations of positive (a) and negative (b) ions in the flames plotted as a function of gas ratios, *R*. The dashed area is the diamond deposition region.

The evolution of the chemical intermediates in the $C_2H_4/C_2H_2/O_2$ combustion flames can be reasonably explained by the kinetic growth mechanism developed by M. Frenklach, in which diamond deposition process is ascribed to a kinetic competition process between diamond and graphite growth.[17] Based on the MS results, diamond films were obtained within a well-defined window of the chemical intermediates as summarized in **Table 5.1**. With a low concentration of etchants and high concentration of hydrocarbon-related intermediates, graphitic carbon was obtained. With a high concentration of etchants and low concentration of hydrocarbons, surface etching or no deposition was resulted. The close correlations of the etchants (H_3O^+ and OH^-) and hydrocarbon-related intermediates ($C_xH_y^+$ and $C_xH_yO^+$) with the deposition behavior suggest their importance in diamond synthesis.

Table 5.1 Relative concentrations of active species in different growth regimes.

Species		Relative concentration (%)		
		Graphite/Amorphous	Diamond	No growth
Positive	H_3O^+	<7.1	7.1-13.5	>13.5
	$C_xH_y^+$	>13.7	11.6-13.7	<11.6
	$C_xH_yO^+$	>6.4	3.9-6.4	<3.9
Negative	OH^-	<2.7	2.7-4.1	>4.1

In summary, the diamond growth and the relative concentration profiles of the chemical intermediates in the flames investigated using MS suggest a well-defined window of the chemical intermediates for effective diamond deposition. Beyond this window, either graphitic carbon deposition (overabundance of hydrocarbon-related intermediates) or no carbon deposition (overabundance of the etching species) was resulted. A balance had to be established between the growth and the etching of diamond and graphitic carbon for producing high-quality diamond at a fast deposition rate.

5. Progress Statement

This research mainly focused on: 1) exploration for alternative energy coupling paths in CVD diamond synthesis; 2) enhancement of diamond deposition; 3) control of crystallographic orientation of diamonds; and 4) identification of active species roles in combustion CVD of diamonds. IR-laser excitations of precursor molecules were used to assist the conventional combustion CVD for modifying the combustion process and promoting the diamond deposition. Mass spectrometric studies of the combustion flame were carried out for in-depth understanding of active species roles in diamond formation.

IR-laser induced vibrational resonant excitations of the CH_2-wagging mode of C_2H_4 molecules were employed to selectively couple the laser energy into the internal motions of the molecular system. Through adjusting the incident laser wavelengths centered at the resonant wavelength, 10.532 μm, on- and off-resonance excitations were finely controlled. On-resonance excitation of C_2H_4 molecules led to: 1) the deposition rate was enhanced by a factor of 5.7; and 2) the diamond quality index factor was improved by 6.05%. On-resonance excitation was found more efficient than off-resonance excitations in modifying the combustion process in a way that increased the flame temperature, promoted the deposition rate, and improved the diamond quality. Optical emission spectroscopic and mass spectrometric studies of the combustion flames revealed that the resonance excitations of C_2H_4 molecules modified the flame chemistry in a way that promoted the production of hydrocarbon species while suppressed the diamond etchant concentration, which is preferred for diamond formation.

Another important step in diamond synthesis is obtaining {100}-textured diamond films, which possess lower surface roughness and higher electronic performance. Laser-induced excitations of one ro-vibrational sub-band head of the CH_2-wagging mode led to {100}-textured diamond film deposition. As the incident laser wavelength was tuned centered at the resonant one, 10.22 μm, the {100}-facet coverage rates were finely controlled. Meanwhile, on-resonance ro-vibrational excitation of C_2H_4 led to a higher deposition rate and a higher diamond quality index factor than off-resonance excitations.

The electronic application of diamonds is greatly limited by the absence of suitable n-typed

diamond. Nitrogen was widely used as n-typed dopant. Nitrogen-containing additives in CVD diamond growth led to severe deterioration of the diamond crystallinity associated with substantial amorphous carbon accumulation. Laser resonant excitations of the NH-wagging mode of NH_3 molecules were employed to combustion CVD of nitrogen-doped diamond films. Drastic morphology transition from an amorphous ball-like structure to a micro-crystalline diamond structure was observed in diamond films prepared with vibrational excitation of NH_3 molecules at a laser wavelength of 9.219 μm. OES and MS of the NH_3-added flames revealed that vibrational excitations of NH_3 modified the flame chemistry in a way that suppressed the concentration of active species, CN, which is detrimental to the diamond crystalline quality.

The diamond growth and the relative concentration profiles of the chemical intermediates in the flames were investigated using MS, which suggested a well-defined window of the chemical intermediates for effective diamond deposition. Beyond this window, either graphitic carbon deposition (overabundance of hydrocarbon-related intermediates) or no carbon deposition (overabundance of the etching species) was resulted. A balance should be established between the growth and the etching of diamond and graphitic carbon for producing high-quality diamond at a fast deposition rate.

6. Refereed References

1) A. C. Ferrari, J. Roberson, "Raman spectroscopy of amorphous, nanostructured, diamond-like carbon, and nanodiamond", Phil Trans R Soc Lond A **362**, 2477 (2004).
2) A. M. Zaitsev, "Optical properties of diamond: a data handbook", (Springer, Berlin; New York, 2001).
3) W. L. Smith and I. M. Mills, "Coriolis perturbations in infrared spectrum of ethylene", J Chem Phys **40**, 2095 (1964).
4) J. S. Kim and M. A. Cappelli, "Temperature measurements in low-pressure, diamond-forming, premixed flames", J Appl Phys **84**, 4595 (1998).
5) J. Asmussen and D. K. Reinhard, Diamond films handbook. (Marcel Dekker, New York, 2002).
6) H. H. Richardson, M. T. Carlson, P. J. Tandler, P. Hernandez and A. O. Govorov, "Experimental and theoretical studies of light-to-heat conversion and collective heating effects in metal nanoparticle solutions", Nano Lett **9**, 1139 (2009).
7) H. J. Fissan, "Temperature distribution in an open air methane-oxygen flame", Combust Flame **17**, 355 (1971).
8) Y. Matsui, A. Yuuki, M. Sahara and Y. Hirose, "Flame structure and diamond growth-mechanism of acetylene torch", Jpn J Appl Phys **28**, 1718 (1989).
9) D. M. Gruen, P. C. Redfern, D. A. Horner, P. Zapol and L. A. Curtiss, "Theoretical studies on nanocrystalline diamond: Nucleation by dicarbon and electronic structure of planar defects", J Phys Chem B **103**, 5459 (1999).
10) N. Uchida, T. Kurita, H. Ohkoshi, K. Uematsu, K. Saito, "Thermochemical etching effect of H2O vapor on CVD diamond film", J Crystal Growth **114**, 565 (1991).

11) A. G. Lowe, A. T. Hartlieb, J. Brand, B. Atakan, and K. Kohse-Hoinghaus, "Diamond deposition in low-pressure acetylene flames: In situ temperature and species concentration measurements by laser diagnostics and molecular beam mass spectrometry", Combustion and Flame **118**, 37 (1999).
12) C. W. David, "IR vibration-rotation spectra of the ammonia molecule", J Chem Educ **73**, 46 (1996).
13) R. L. Stolk, M. M. J. W. van Herpen, J. J. Schermer and J. J. ter Meulen, "Influence of nitrogen addition on oxyacetylene flame chemical vapor deposition of diamond as studied by solid state techniques and gas phase diagnostics", J Appl Phys **93**, 4909 (2003).
14) T. M. Hong, S. H. Chen, Y. S. Chiou and C. F. Chen, "Optical emission spectroscopy studies of the effects of nitrogen addition on diamond synthesis in a CH_4-CO_2 gas-mixture", Appl Phys Lett **67**, 2149 (1995).
15) A. N. Hayhurst, and D. B. Kittelson, "The positive and negative ions in oxy-acetylene flame", Combustion and Flame **31**, 37 (1978).
16) A. V. Orden, and R. J. Saykally, "Small carbon clusters: spectroscopy, structure, and energetics", Chem. Rev. **98**, 2313 (1998).
17) M. Frenklach, and K. E. J. Spear, "Growth mechanism of vapor-deposited diamond", Mater. Res. **3**, 133 (1988).
18) A. N. Hayhust, and N. R. Telford, "Kinetics and heats of the reactions H+ H + OH $\leftrightarrow$ $H_3O^+ + e^-$ in flames", Nature-Phys. Sci. **235**, 114 (1972).
19) Y. Hirose, S. Amanuma, "The synthesis of high-quality diamond in combustion flames", J. Appl. Phys. **68**, 6401 (1990).
20) L. S. Fan, Y. S. Zhou, M. X. Wang, Y. Gao, L. Liu, J. F. Silvain, and Y. F. Lu, "Resonant vibrational excitation of ethylene molecules in laser-assisted diamond deposition", Laser Phyics Letter **11**, 076002 (2014).
21) L.S. Fan, Z.Q. Xie, J.B. Park, X.N. He, Y.S. Zhou, L. Jiang, and Y.F. Lu, "Synthesis of nitrogen-doped diamond films using vibrational excitation of ammonia molecules in laser-assisted combustion flames", Journal of Laser Applications, 24(2), 022001, 2012.